THE SL2S GALAXY-SCALE LENS SAMPLE. IV. THE DEPENDENCE OF THE TOTAL MASS DENSITY PROFILE OF EARLY-TYPE GALAXIES ON REDSHIFT, STELLAR MASS, AND SIZE

Alessandro Sonnenfeld 1* , Tommaso Treu 1† , Raphaël Gavazzi 2 , Sherry H. Suyu 1,3,4 , Philip J. Marshall 5,3 , Matthew W. Auger 6 , and Carlo Nipoti 7

Draft version February 1, 2018

ABSTRACT

We present optical and near infrared spectroscopy obtained at Keck, VLT, and Gemini for a sample of 36 secure strong gravitational lens systems and 17 candidates identified as part of the SL2S survey. The deflectors are massive early-type galaxies in the redshift range $z_d = 0.2 - 0.8$, while the lensed sources are at $z_s = 1 - 3.5$. We combine this data with photometric and lensing measurements presented in the companion paper III and with lenses from the SLACS and LSD surveys to investigate the cosmic evolution of the internal structure of massive early-type galaxies over half the age of the universe. We study the dependence of the slope of the total mass density profile γ' ($\rho(r) \propto r^{-\gamma'}$) on stellar mass, size, and redshift. We find that two parameters are sufficent to determine γ' with less than 6% residual scatter. At fixed redshift, γ' depends solely on the surface stellar mass density $\partial \gamma'/\partial \Sigma_* = 0.38 \pm 0.07$, i.e. galaxies with denser stars also have steeper slopes. At fixed M_* and $R_{\rm eff}$, γ' depends on redshift, in the sense that galaxies at a lower redshift have steeper slopes $(\partial \gamma'/\partial z)$ -0.31 ± 0.10). However, the mean redshift evolution of γ' for an individual galaxy is consistent with zero $d\gamma'/dz = -0.10 \pm 0.12$. This result is obtained by combining our measured dependencies of γ' on z, M_*, R_{eff} with the evolution of the R_{eff} - M_* taken from the literature, and is broadly consistent with current models of the formation and evolution of massive early-type galaxies. Detailed quantitative comparisons of our results with theory will provide qualitatively new information on the detailed physical processes at work.

Subject headings: galaxies: fundamental parameters — gravitational lensing —

1. INTRODUCTION

The formation and evolution of early-type galaxies (ETGs) is still an open question. Though frequently labeled as "red and dead" and traditionally thought to form in a "monolithic collapse" followed by "passive" pure luminosity evolution, in the past decade a far more complicated history has emerged (e.g., Renzini 2006, and references therein). ETGs are thought to harbor supermassive black holes at their centers (Ferrarese & Merritt 2000; Gebhardt et al. 2000) which regulate the conversion of gas into stars (De Lucia et al. 2006). Traces of recent star formation are ubiquitously found when sensitive diagnostics are applied (Treu et al. 2002; Kaviraj Episodes of tidal disturbances and interactions with other systems occur with remarkable frequency even at recent times (e.g. Malin & Carter 1983; van Dokkum 2005; Tal et al. 2009; Atkinson et al. 2013).

Their structural properties evolve in the sense that their sizes appear to grow with time at fixed stellar mass (van Dokkum et al. 2008; Damjanov et al. 2011; Newman et al. 2012; Huertas-Company et al. 2013; Carollo et al. 2013). The mode of star formation seems to be different from that found in spiral galaxies, resulting in a different stellar initial mass function (Treu et al. 2010; van Dokkum & Conroy 2010; Auger et al. 2010b; Brewer et al. 2012; Cappellari et al. 2013). Finally, from a demographic point of view, their number density has been found to have evolved significantly since $z \sim 2$ (e.g., Ilbert et al. 2013).

Reproducing these observations is an enormous challenge for theoretical models. Major and minor mergers are thought to be the main processes driving their structural and morphological evolution, but it is not clear if they can account for the observed evolution while reproducing all the observables (Nipoti et al. 2009a; Hopkins et al. 2010; Oser et al. 2012; Remus et al. 2013).

Gravitational lensing, by itself and in combination with other probes, can be used to great effect to measure the mass profiles of early-type galaxies, both in the nearby universe and at cosmological distances (Treu & Koopmans 2002a,b; Rusin et al. 2003; Treu & Koopmans 2004; Rusin & Kochanek 2005; Koopmans et al. 2006; Jiang & Kochanek 2007; Gavazzi et al. 2007; Auger et al. 2010a; Lagattuta et al. 2010). Until recently, however, this approach was severely limited by the small size of the known samples of strong gravitational lenses. This has motivated a number of dedicated searches which have, in the past decade, increased the sample of known strong

 $^{1}\,\mathrm{Physics}$ Department, University of California, Santa Barbara, CA 93106, USA

France 4 Institute of Astronomy and Astrophysics, Academia Sinica, P.O. Box 23-141, Taipei 10617, Taiwan

⁶ Institute of Astronomy, University of Cambridge, Madingley Rd, Cambridge, CB3 0HA, UK

Astronomy Department, University of Bologna, via Ranzani 1, I-40127 Bologna, Italy

² Institut d'Astrophysique de Paris, UMR7095 CNRS - Université Pierre et Marie Curie, 98bis bd Arago, 75014 Paris, France

³ Kavli Institute for Particle Astrophysics and Cosmology, Stanford University, 452 Lomita Mall, Stanford, CA 94305, USA ⁵ Department of Physics, University of Oxford, Keble Road, Oxford, OX1 3RH, UK

^{*} sonnen@physics.ucsb.edu

[†] Packard Research Fellow

gravitational lens systems by more than an order of magnitude (e.g., Browne et al. 2003; Bolton et al. 2008; Faure et al. 2008; Treu et al. 2011).

2

In spite of all this progress the number of known lenses at $z \sim 0.5$ and above is still a severe limitation. Increasing this sample and using it as a tool to understand the formation and evolution of massive galaxies is the main goal of our SL2S galaxy-scale lens search (Gavazzi et al. 2012) and other independent searches based on a variety of methods (Brownstein et al. 2012; Marshall et al. 2009; Negrello et al. 2010; Pawase et al. 2012; Inada et al. 2012; González-Nuevo et al. 2012; Wardlow et al. 2013; Vieira et al. 2013).

In our pilot SL2S paper (Ruff et al. 2011) we measured the evolution of the density slope of massive early-type galaxies by combining lensing and dynamics measurements of a sample of just 11 SL2S lenses with similar measurements taken from the literature (Treu & Koopmans 2004; Koopmans et al. 2009; Auger et al. 2010b), finding tentative evidence that the density profile of massive ETGs steepens with cosmic time on average. This trend was later confirmed qualitatively by an independent study of Bolton et al. (2012) and agrees with the theoretical work by Dubois et al. (2013). However, the picture is not clear: the observed trend is tentative at best, while different theoretical studies find contrasting evolutionary trends (Johansson et al. 2012; Remus et al. 2013). More data and better models are needed to make progress.

In order to clarify the observational picture, we have collected a much larger sample of objects, more than tripling the sample of secure lenses with all the necessary measurements, with respect to our pilot study. Photometric and strong lensing measurements for this expanded sample are presented in a companion paper (Sonnenfeld et al. 2013, hereafter Paper III). In this paper we present spectroscopic data for the same objects. Deflector and source redshifts are used to convert the geometry of the lens system into measurements of a physical mass within a physical aperture. Stellar velocity dispersions are used as an independent constraint on the gravitational potential of the lens, allowing for more diagnostic power on the structure of our targets.

The combination of the photometric, lensing, and spectroscopic data is used in this paper to study the cosmic evolution of the slope of the average mass density profile of massive early-type galaxies. This is achieved by fitting power law density profiles $(\rho(r) \propto r^{-\gamma'}; \gamma' \approx 2)$ in the local universe) to the measured Einstein radii and velocity dispersions of our lenses. Such a measurement of γ' is a good proxy for the mean density slope within the effective radius. The goal of this paper is to measure trends of γ' with redshift, in continuity with our previous work (Ruff et al. 2011), as well as with other structural properties of massive ETGs, such as stellar mass and size. Such measurements will help us understand the structural evolution of ETGs from z=0.8 to present times.

This paper is organized as follows. We briefly summarize the relevant features of the SL2S galaxy scale lens sample in Section 2, and show in detail the spectroscopic data set and the measurements of redshifts and velocity dispersions of our lenses in Section 3. In Section 4

TABLE 1 Census of SL2S lenses.

Grade	Α	В	С	Χ	Total
With high-res imaging With spectroscopy High-res imaging and spectroscopy Total with follow-up	30	3	13	21	67
	36	15	2	5	58
	27	3	0	0	30
	39	15	15	26	95

Note. — Number of SL2S candidates for which we obtained follow-up observations in each quality bin. Grade A: definite lenses, B: probable lenses, C: possible lenses, X: non-lenses. We differentiate between lenses with spectroscopic follow-up, high-resolution imaging follow-up or any of the two.

we discuss the properties of SL2S lenses in relation with lenses from independent surveys. In Section 5 we briefly explain how lensing and kinematics measurements are combined to infer the density slope γ' and discuss the physical meaning of such measurements. In Section 6 we combine individual γ' measurements to infer trends of this parameter across the population of ETGs. After a discussion of our results in Section 7 we conclude in Section 8.

Throughout this paper magnitudes are given in the AB system. We assume a concordance cosmology with matter and dark energy density $\Omega_m=0.3,~\Omega_{\Lambda}=0.7,$ and Hubble constant $H_0{=}70~{\rm km~s^{-1}Mpc^{-1}}.$

2. THE SAMPLE

The gravitational lenses studied in this paper were discovered as part of the Strong Lensing Legacy Survey (Cabanac et al. 2007, SL2S) with a procedure described in detail in Gavazzi et al. (2012). Lens candidates are identified in imaging data from the CFHT Legacy Survey and then followed up with Hubble Space Telescope (HST) high resolution imaging and/or spectroscopy. In Paper III we ranked the candidates, assigning them a grade indicating their likelihood of being strong lenses, with the following scheme: grade A for definite lenses, grade B for probable lenses, grade C for possible lenses and grade X for non-lenses. A summary with the number of systems in each category is given in Table 1. In this paper we analyze all lenses with spectroscopic data that have not been ruled out as grade X systems.

3. SPECTROSCOPIC OBSERVATIONS

The SL2S spectroscopic campaign was started in 2006. The goal of our spectroscopic observations is to measure the lens and source redshifts and lens velocity dispersion for all our systems. Different telescopes (Keck, VLT and Gemini), instruments (LRIS, DEIMOS, X-Shooter, GNIRS) and setups have been used to achieve this goal, reflecting technical advances during the years and the optimization of our strategy. In what follows we describe the procedure used to measure the three key spectroscopic observables. A summary of all measurements is given in Table 2.

3.1. Deflector redshifts and velocity dispersions

The typical brightness of our lenses is around $i \sim 20$. With an 8m class telescope, their redshift can be measured from their optical absorption lines with ~ 10 minutes of exposure time, while a measurement of their velocity dispersion typically takes from 30 to 120 minutes.

Optical spectroscopy data come from three different instruments.

For most of the systems we have data obtained with the LRIS spectrograph at Keck (Oke et al. 1995). The wavelength coverage of LRIS is typically in the range 3500-8000 Å for data taken before 2009 and extends up to 10000 Å for later data, after the installation of the new detector with much reduced fringing patterns (Rockosi et al. 2010). The spectral resolution is about 140 km s⁻¹ FWHM on the red side of the spectrograph. Data reduction for LRIS spectra was performed with a pipeline written by M.W. Auger.

For a set of 13 systems we have VLT observations with the instrument X-Shooter 10 . X-Shooter has both a higher resolution ($\sim 50\,\mathrm{km\,s^{-1}}$) and a longer wavelength coverage (from 3500 Å up to 25000 Å) than LRIS. X-Shooter spectra were reduced with the default ESO pipeline 11 . The observations were done by nodding along a long slit of width 0'.9 for the UVB and VIS arms and 1'.0 for the NIR arm.

Finally, six systems presented here have data obtained with DEIMOS at Keck (Faber et al. 2003). The grating used in all DEIMOS observations is the 600ZD, with a wavelength range between 4500 Å and 9500 Å and a spectral resolution of about $160\,\mathrm{km\,s^{-1}}$. DEIMOS data were reduced with the DEEP2 pipeline (Cooper et al. 2012; Newman et al. 2012).

Both redshifts and velocity dispersions are measured by fitting stellar templates, broadened with a velocity kernel, to the observed spectra. This is done in practice with a Monte Carlo Markov Chain adaptation of the velocity dispersion fitting code by van der Marel (1994), written by M. W. Auger and described by Suyu et al. (2010). We used 7 different templates of G and F stars, which should provide an adequate description of the stars in red passive galaxies, taken from the Indo US stellar library. The code also fits for an additive polynomial continuum, to accommodate for template mismatch effects or imperfections in the instrumental response correction. In most cases, a polynomial of order five is used.

The rest-frame wavelength range typically used in our fits is $3850\mbox{\ensuremath{\mathring{A}}}-5250\mbox{\ensuremath{\mathring{A}}}$, which brackets important absorption lines such as Ca K,H at $3934,3967\mbox{\ensuremath{\mathring{A}}}$, the G-band absorption complex around $4300\mbox{\ensuremath{\mathring{A}}}$ and Mgb at $5175\mbox{\ensuremath{\mathring{A}}}$. Depending on the redshift of the target and the instrument used, this is not always allowed as part of the wavelength region can fall outside the spectral coverage allowed by the detector, or because of Telluric absorption. In those cases the fitted rest-frame region is extended.

Systematic uncertainties in the velocity dispersion measurements are estimated by varying the fitted wavelength region and order of the polynomial continuum. These are typically on the order of $20~\rm km\,s^{-1}$ and are then summed in quadrature to the statistical uncertainty.

All the optical spectra of our systems are shown in Figure 1.

3.2. Source spectroscopy

¹⁰ ESO/VLT programs 086.B-0407(A) and 089.B-0057(A), PI

Measuring the redshift of a lensed background source is important not only for determining the geometry of the gravitational lens system, but also to confirm that the arc is actually in the background relative to the lens. The arcs of the lensed sources are relatively faint in broad band photometry $(q \sim 24)$, implying that their continuum radiation cannot be detected in most cases. However the sources are selected to be blue (Gavazzi et al. 2012) and are often associated with emission lines from star formation and/or nuclear activity. The typical redshifts of our arcs are in the range 1 < z < 3. This means that optical spectroscopy can effectively detect emission from the [OII] doublet at 3727 - 3729 Å, for the lowest redshift sources, or Ly- α for objects at z > 2.5 or so. This is the case for roughly half of the systems observed. The remaining half does not show detectable emission line in the observed optical part of the spectrum, either because the most important lines fall in the near-infrared. or because emission is too weak. Emission lines from the arcs can be easily distinguished by features in the lens because they are spatially offset from the lens light.

X-Shooter observations proved to be remarkably efficient in measuring source redshifts. This is in virtue of its wavelength range that extends through the near infrared up to 25000Å and its medium resolution that limits the degrading effect of emission lines from the atmosphere. Of 13 systems observed with X-Shooter, 12 of them yielded a redshift of the background source, all of which with at least two identified lines.

In addition, for four systems we have near infrared spectroscopic observations with the instrument GNIRS on Gemini North (PI Marshall, GN-2012B-Q-78, PI Sonnenfeld, GN-2013A-Q-91), used in cross-dispersed mode, covering the wavelength range $10000\mbox{\ensuremath{\ensuremath{A}}}-25000\mbox{\ensuremath{\ensuremath{A}}}$ at once. Of the four systems observed, two of them show two emission lines from the background source.

In most cases when only optical spectroscopy is available, only one emission line is detected over the whole spectrum. The [OII] doublet can be easily identified even with relatively low resolution spectrographs. The identification of the Ly- α line is less trivial. Ly- α is typically the brightest emission line in the rest frame wavelength range 1000 - 3000 Å when present, but other emission lines like CIV 1546Å, OIII 1666Åor CIII 1908Å can sometimes be seen. When we detect an emission line close to the blue end of the spectrum it could in principle be any of those lines. However a detection of one of the above lines and a non-detection of the other ones is quite unlikely, unless CIII 1908Å falls right at the blue edge of the observed spectrum. In that case though we should expect to observe the OII doublet at redder wavelengths. This case is never encountered, therefore in all cases when we detect an unresolved emission line bluer than 6000Å, and no other lines, we can safely assume it is Ly- α . The system SL2SJ022357-065142 is a particular case: we detected an emission line spatially associated with the background source at 9065Å, with a $5-\sigma$ significance. Given the low S/N the line is both compatible with being the OII doublet or an individual line. Possible other lines are OIII 5007Åand H- β , which cannot be ruled out. Therefore we do not claim redshift measurements for that source: deeper data is needed to establish

¹¹ http://www.eso.org/sci/facilities/paranal/instruments/xshoowengther the line is the OII doublet or not.

The 2d spectra around all the detected emission lines for all the systems are shown in Figure 3. Note that for some systems the line emission is multiply imaged on both sides of the foreground object. This provides a decisive clue on the lens nature of those systems, important when ranking our targets by their likelihood of being lenses (Paper III).

Finally, six background sources are bright enough to be visible with continuum radiation and several absorption/emission features can be identified in their spectra. The absorption line spectra of these sources are plotted in Figure 2.

Despite our efforts in acquiring spectroscopic data for our lenses, seven of the 36 grade A lenses with spectroscopic follow-up have no measured source redshifts. In Paper II Ruff et al. (2011) made use of photometric data together with lensing cross-section arguments to estimate source redshifts, with a technique called *photogeometric redshift*. Here the fraction of lenses with no source redshift is small compared to the sample size, therefore it is not essential to include them in the analysis through the use of this method.

4. SAMPLE CHARACTERIZATION

In Paper III we presented effective radii, magnitudes, stellar masses and Einstein radii of our lenses. Here we complement this information with lens and source redshifts, and lens velocity dispersions. It is possible at this point to look at the distribution of our lenses in the parameter space defined by these quantities. Since our scientific goal is to measure the evolution in the mean density slope with time, it is very important to assess whether other observables appear to evolve in our sample. In Figure 4 we plot the effective radii, stellar masses and velocity dispersions as a function of redshift for all our objects, and also for lenses from other surveys. Throughout this paper, when dealing with stellar masses we refer to values measured from stellar population synthesis fitting based on a Salpeter initial mass function (IMF). For a fair comparison, all velocity dispersions, which are measured within rectangular apertures of arbitrary sizes, are transformed into velocity dispersions within a circular aperture, $\sigma_{\rm e2}$, with radius $R_{\rm eff}/2$ following the prescription of Jørgensen et al. (1995). The values of σ_{e2} for individual SL2S lenses are reported in Table 4.

SL2S lenses do not appear to differ from objects from independent lensing surveys in the average values of $R_{\rm eff}$, M_* and $\sigma_{\rm e2}$. As far as trends with redshift within the SL2S sample are concerned, there is a mild increase of the stellar mass with z that will need to be taken into account when discussing the evolution of the mass profile of these objects.

As an additional test, we examine the correlation between mass and effective radius for SL2S, SLACS and LSD lenses and check it against non-lens galaxies. The goal is to make sure that these surveys do not preferentially select lenses with a larger or smaller size than typical ETGs of their mass. The mass-radius relation is seen to evolve with time (e.g. Damjanov et al. 2011; Newman et al. 2012; Cimatti et al. 2012). We correct for this evolution by considering effective radii evolved to z=0 assuming the trend measured by Newman et al. (2012): $\log R_{\rm eff}(z=0) = \log R_{\rm eff} + 0.26z$. Effective radii

defined in this way are plotted against measured stellar masses in Figure 5, together with the mass-radius relation measured by Newman et al. (2012) for low-redshift SDSS galaxies. Points in the plot of Figure 5 should not be considered as evolutionary tracks of individual objects, as galaxies grow in mass as well as in size. For a given object, its redshift-evolved size $R_{\text{eff}}(z=0)$ is equivalent to its measured effective radius rescaled by the average size of galaxies at its redshift and at a reference mass. This allows us to promptly display in a single plot how our lenses compare, in terms of size, to other galaxies of the same mass, regardless of redshift. We see from Figure 5 that lenses from all surveys lie nicely around the relation found for non-lenses, indicating that our sample of lenses does not appear special when compared to the more general population of galaxies of their redshift.

5. POWER LAW MODELS

We now proceed to combine lensing measurements with stellar kinematics information to infer the total mass density profile of each lens galaxy. We follow the now standard procedure in lensing and dynamics studies (Treu & Koopmans 2002a), as used by Ruff et al. (2011). We model the total (dark matter + stars) mass profile as a spherical power law $\rho(r) \propto r^{-\gamma'}$ in the kinematic analysis. The free parameters of the model are the slope γ' , and the mass normalization. For a given model we calculate the line of sight velocity dispersion within the rectangular aperture of our observation, broadened by the seeing, through the spherical Jeans equation. We assume isotropic orbits and a de Vaucouleurs profile for the distribution of tracers (de Vaucouleurs 1948), with effective radius fixed to the observed one. We then compare the model to the observed velocity dispersion and Einstein radius to derive posterior probability densities for the free parameters. In spite of the clear approximations, the method has been shown to be very robust when compared to results of more sophisticated models (e.g. Barnabè et al. 2011).

The data required for this inference are the Einstein radius of the lens, the redshift of both the deflector galaxy and the lensed source, and the velocity dispersion of the lens. Of the 39 grade A lenses of the SL2S sample, 25 have all the required data. For the few systems with two or more independent measurements of the velocity dispersion, we use the weighted average. The inferred values of γ' are reported in Table 4.

5.1. The meaning of γ'

Before analyzing the measurements in a statistical sense we need to understand what physical properties the quantity γ' is most sensitive to. Observations (Sonnenfeld et al. 2012) and simple arguments (galaxies have a finite mass) suggest that the true density profile deviates from a pure power law, particularly at large radii. Thus our power law fits to the lensing and kinematics data must be interpreted as an approximation of the average density slope over a radial range explored by our data. Since for a typical lens both the Einstein radius and the velocity dispersion probe the region within the effective radius, we expect that the inferred γ' will be close to the mean density slope within $R_{\rm eff}$, as suggested by Dutton & Treu (2013).

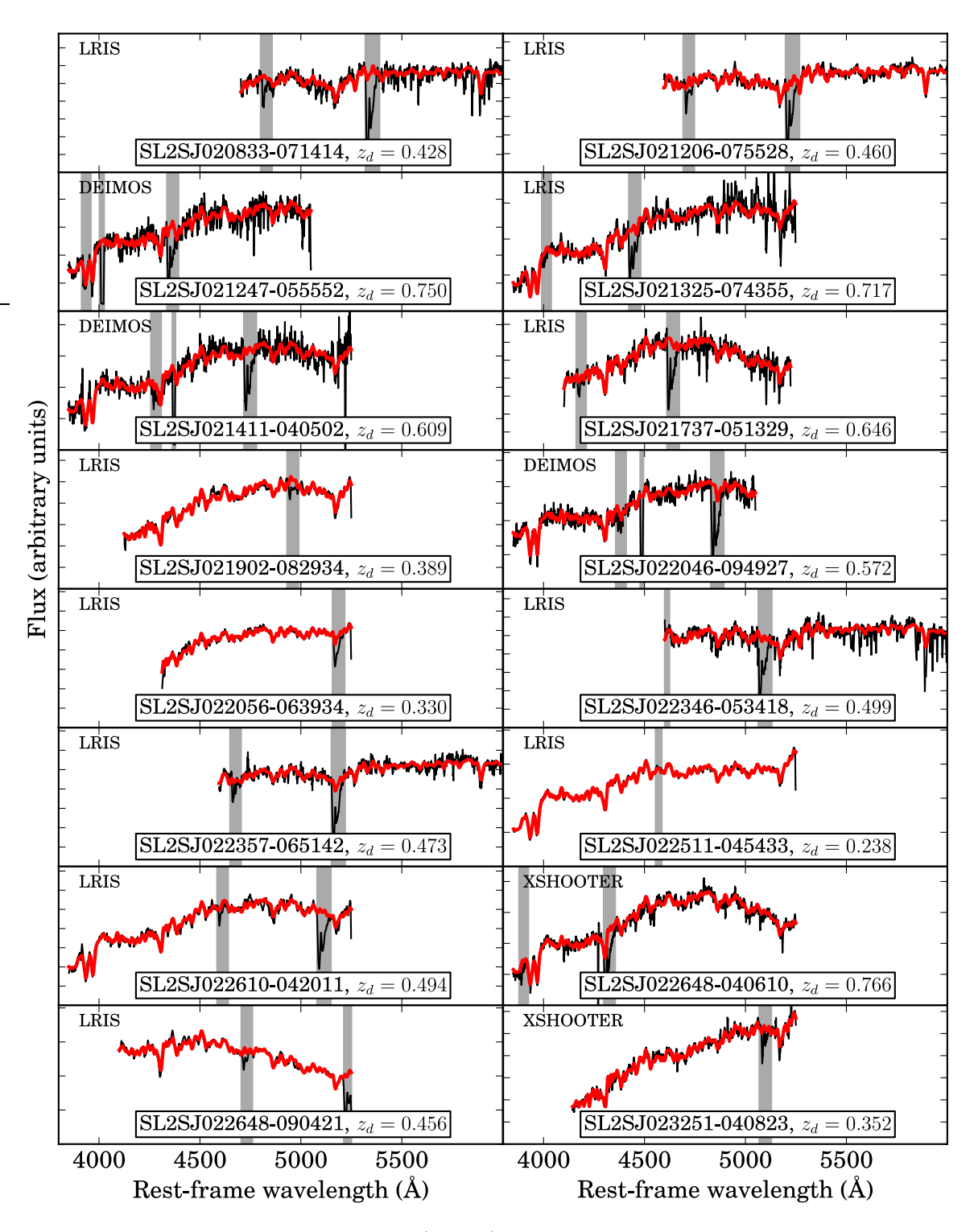


Fig. 1.— 1d spectra of SL2S lenses and lens candidates (in black). Where available, we overplot the best fit spectrum obtained for the velocity dispersion fitting (in red). Only the rest-frame wavelength region used in the fit is shown. Vertical gray bands are regions of the spectrum masked out of the fit and typically correspond to atmospheric absorption features. Each plot indicates the redshift of the galaxy and the instrument used to acquire the data shown.

TABLE 2 SPECTROSCOPIC OBSERVATIONS.

Name	obs. date	Instrument	slit (")	width $('')$	seeing $('')$	exp. time (s)	z_d	z_s	σ (km/s)	$_{(\mathring{A}^{-1})}^{S/N}$	res. (km/s
SL2SJ020833-071414	11-29-2011	LRIS	1.0	1.62	1.0	900	0.428		295 ± 27	17	150
SL2SJ021206-075528	01-28-2011	LRIS	0.7	1.62	0.6	2700	0.460		257 ± 25	28	120
SL2SJ021247-055552	10-08-2010	XSHOOTER	0.9	1.60	0.7	2800	0.750	2.74	273 ± 22	22	47
	12-09-2012	DEIMOS	1.0	1.90	1.2	3600			253 ± 28	11	170
SL2SJ021325-074355	09-14-2007	LRIS	1.0	1.68	0.6	1800	0.717	3.48	293 ± 34	5	220
SL2SJ021411-040502	12-09-2012	DEIMOS	1.0	1.88	0.8	3600	0.609	1.88	287 ± 47	10	170
	01-28-2011	LRIS	0.7	1.62	0.6	2700			264 ± 26	13	120
	10-08-2010	XSHOOTER	0.9	1.60	0.7	2800			209 ± 20	27	49
SL2SJ021737-051329	12-23-2006	LRIS	1.5	1.68	0.6	2400	0.646	1.85	239 ± 27	11	160
	09-14-2007	LRIS	1.0	1.68	0.6	3600			292 ± 33	12	120
SL2SJ021801-080247	01-28-2011	LRIS	0.7	1.62	0.6	1800		2.06		6	120
	12-09-2012	DEIMOS	1.0	0.81	1.0	1200				5	170
SL2SJ021902-082934	09-13-2007	LRIS	1.0	1.68	0.7	2700	0.389	2.15	289 ± 23	21	210
SL2SJ022046-094927	12-09-2012	DEIMOS	1.0	1.90	0.8	1800	0.572		254 ± 29	10	170
SL2SJ022056-063934	09-13-2007	LRIS	1.0	1.68	0.8	1800	0.330		231 ± 25	23	220
SL2SJ022346-053418	11-30-2011	LRIS	1.0	1.62	0.6	900	0.499	1.44	288 ± 28	20	140
SL2SJ022357-065142	08-06-2010	LRIS	1.0	1.64	1.0	900	0.473		312 ± 27	23	160
	11-01-2010	LRIS	1.0	1.64	0.9	900	0.2.0		289 ± 28	25	150
SL2SJ022511-045433	09-09-2009	LRIS	1.0	0.81	0.7	1800	0.238	1.20	234 ± 21	54	500
SL2SJ022610-042011	09-14-2007	LRIS	1.0	1.62	0.6	1800	0.494	1.23	263 ± 24	15	230
SL2SJ022648-040610	12-23-2006	LRIS	1.5	1.68	0.6	2700	0.766		333 ± 24	9	160
010010	10-08-2010	XSHOOTER	0.9	1.60	0.6	2800	0.100		324 ± 21	43	47
SL2SJ022648-090421	09-14-2007	LRIS	1.0	1.68	0.6	1800	0.456		302 ± 24	23	220
SL2SJ023251-040823	09-13-2007	LRIS	1.0	1.68	0.7	2700	0.352	2.34	281 ± 26	19	220
02200020201 010020	10-06-2010	XSHOOTER	1.0	1.60	0.7	2800	0.002	2.01	247 ± 32	37	49
SL2SJ084847-035103	01-03-2011	XSHOOTER	0.9	1.60	1.0	2800	0.682	1.55	197 ± 21	19	49
SL2SJ084909-041226	01-02-2011	XSHOOTER	0.9	1.60	0.9	2800	0.722	1.54	320 ± 24	14	49
02200001000 011220	12-09-2012	DEIMOS	1.0	1.88	0.8	6000	0	1.01	275 ± 26	26	160
SL2SJ084934-043352	01-28-2011	LRIS	0.7	1.62	0.6	1800	0.373		245 ± 24	23	120
SL2SJ084959-025142	01-01-2011	XSHOOTER	0.9	1.60	0.8	2800	0.274	2.09	276 ± 35	67	47
SL2SJ085019-034710	01-28-2011	LRIS	0.7	1.62	0.6	2700	0.337	3.25	290 ± 24	26	120
SL2SJ085327-023745	11-30-2011	LRIS	1.0	1.62	0.9	4800	0.774	2.44	200 ± 21		150
SL2SJ085540-014730	01-28-2011	LRIS	0.7	1.62	0.6	3600	0.365	3.39	222 ± 25	24	120
2220000010 011700	12-09-2012	DEIMOS	1.0	1.88	0.8	2400	0.000	0.00	209 ± 31	14	160
SL2SJ085559-040917	01-28-2011	LRIS	0.7	1.62	0.6	3600	0.419	2.95	281 ± 22	33	120
SL2SJ085826-014300	11-30-2011	LRIS	1.0	1.62	0.0	3600	0.580	2.30	231 ± 25 233 ± 25		160
SL2SJ090106-025906	01-07-2011	XSHOOTER	0.9	1.60	0.7	2800	0.670	1.19	200 ± 20	7	49
SL2SJ090407-005952	12-30-2010	XSHOOTER	0.9	1.60	0.7	2800	0.611	2.36	183 ± 21	22	52
SL2SJ095921+020638	02-02-2011	XSHOOTER	0.9	1.60	0.7	2800	0.552	3.35	188 ± 22	17	47
SL2SJ135847+545913	04-29-2011	LRIS	1.0	1.62	0.7	2700	0.552 0.510		287 ± 22	28	150
21200100017040310	03-22-2011	GNIRS	0.675	1.02	0.3	7200	0.010		201 ± 22		100
SL2SJ135949+553550	03-22-2013	LRIS	1.0	1.62	$0.7 \\ 0.7$	5400	0.783	2.77	228 ± 29	9	150
OU4001100949+000000	04-29-2011	LRIS	1.0	$\frac{1.02}{1.62}$	0.7	5400	0.100	4.11	228 ± 29 234 ± 28	9 12	150
SL2SJ140123+555705	07-20-2006	LRIS	1.0 1.5	3.36	0.9	1200	0.527		234 ± 26 332 ± 25	10	210
SL2SJ140125+555705 SL2SJ140156+554446	04-29-2011	LRIS	1.0	$\frac{3.30}{1.62}$	0.8	2700	0.327 0.464		332 ± 23 297 ± 22	34	150
シロをいす 140190十つり4440	U4-43-2U11	LITIS	1.0	1.02	0.0	4100	0.404		231 I 22	54	190

 $\ensuremath{\mathsf{Note}}.$ — Summary of spectroscopic observations and derived parameters.

Name	obs. date	Instrument	slit (")	$_{('')}^{\mathrm{width}}$	seeing $('')$	exp. time (s)	z_d	z_s	σ (km/s)	$_{(\mathring{A}^{-1})}^{S/N}$	$\frac{\text{res.}}{(\text{km/s})}$
SL2SJ140454+520024	04-30-2011	LRIS	1.0	1.62	0.9	1800	0.456	1.59	342 ± 20	38	140
SL2SJ140546+524311	04-29-2011	LRIS	1.0	1.62	0.8	2700	0.526	3.01	284 ± 21	30	140
	03-26-2013	GNIRS	0.675		0.5	4800					
SL2SJ140614+520253	07-20-2006	LRIS	1.5	3.36	0.8	1200	0.480		247 ± 29	11	190
SL2SJ140650+522619	04-29-2011	LRIS	1.0	1.62	0.9	3600	0.716	1.47	253 ± 19	15	150
	04-30-2011	LRIS	1.0	1.62	0.9	3600			247 ± 20	16	160
SL2SJ141137+565119	01-14-2010	LRIS	1.0	1.62	1.3	2700	0.322	1.42	214 ± 23	35	470
SL2SJ142003+523137	04-30-2011	LRIS	1.0	1.62	0.9	2700	0.354	1.41		4	150
SL2SJ142031+525822	04-29-2011	LRIS	1.0	1.62	0.8	1800	0.380	0.99	246 ± 23	24	150
SL2SJ142059+563007	04-29-2011	LRIS	1.0	1.62	0.9	1800	0.483	3.12		20	
	04-30-2011	LRIS	1.0	1.62	0.8	1800			228 ± 19	18	160
SL2SJ142731+551645	04-30-2011	LRIS	1.0	1.62	0.8	3600	0.511	2.58		12	150
SL2SJ220329+020518	08-06-2010	LRIS	1.0	1.62	0.9	2700	0.400	2.15	213 ± 21	36	170
SL2SJ220506+014703	10-06-2010	XSHOOTER	0.9	1.60	0.8	2800	0.476	2.53	317 ± 30	29	49
SL2SJ220629+005728	09-13-2007	LRIS	1.0	1.68	0.7	2700	0.704		290 ± 39	6	230
SL2SJ221326-000946	09-09-2009	LRIS	1.0	1.62	1.0	1800	0.338	3.45	165 ± 20	30	150
	07-29-2011	XSHOOTER	0.9	1.60	0.8	2800			177 ± 21	32	56
SL2SJ221407-180712	09-13-2007	LRIS	1.0	1.68	0.7	2700	0.651		200 ± 24	6	220
SL2SJ221852+014038	08-06-2010	LRIS	1.0	1.62	0.9	2700	0.564		305 ± 23	28	170
	11-10-2012	GNIRS	0.675		0.7	3600					
SL2SJ221929-001743	09-14-2007	LRIS	0.7	1.68	0.6	1800	0.289	1.02	189 ± 20	23	420
SL2SJ222012+010606	08-18-2012	DEIMOS	1.0	1.88	1.2	3600	0.232	1.07	127 ± 15	14	170
SL2SJ222148+011542	11-11-2012	GNIRS	0.675		0.7	3600	0.325	2.35			
	08-18-2012	DEIMOS	1.0	1.88	1.2	3600			222 ± 23	25	160
	10-01-2012	XSHOOTER	0.9	1.60	1.0	1400					
SL2SJ222217+001202	08-06-2010	LRIS	1.0	1.62	0.9	900	0.436	1.36	221 ± 22	13	170
	11-01-2010	LRIS	1.0	1.62	0.9	900			200 ± 29	10	150

 $\ensuremath{\mathsf{Note}}.$ — Summary of spectroscopic observations and derived parameters.

TABLE 3 LENSING AND DYNAMICS.

Name	z_d	R_{eff} (kpc)	$R_{\rm Ein}$ (kpc)	σ_{e2} (km s ⁻¹)	$\log M_*^{\rm Salp}/M_{\odot}$	γ'	Notes
SL2SJ021247-055552	0.750	8.92	9.33	267 ± 17	11.45 ± 0.17	2.05 ± 0.09	
SL2SJ021325-074355	0.717	17.67	17.22	287 ± 33	11.97 ± 0.19	1.79 ± 0.12	
SL2SJ021411-040502	0.609	6.29	9.48	238 ± 15	11.60 ± 0.14	1.85 ± 0.07	
SL2SJ021737-051329	0.646	4.27	8.80	270 ± 21	11.53 ± 0.16	2.02 ± 0.09	
SL2SJ021902-082934	0.389	3.01	6.88	300 ± 23	11.50 ± 0.10	2.26 ± 0.08	
SL2SJ022511-045433	0.238	8.59	6.65	226 ± 20	11.81 ± 0.09	1.78 ± 0.10	
SL2SJ022610-042011	0.494	6.44	7.23	266 ± 24	11.73 ± 0.11	2.01 ± 0.12	
SL2SJ023251-040823	0.352	4.78	5.15	271 ± 20	11.36 ± 0.09	2.39 ± 0.10	
SL2SJ084847-035103	0.682	3.21	6.02	205 ± 21	11.24 ± 0.16	1.84 ± 0.13	
SL2SJ084909-041226	0.722	3.55	7.94	312 ± 18	11.63 ± 0.13	2.14 ± 0.07	
SL2SJ084959-025142	0.274	6.11	4.84	275 ± 34	11.52 ± 0.09	2.33 ± 0.17	
SL2SJ085019-034710	0.337	1.35	4.48	307 ± 25	11.14 ± 0.09	2.45 ± 0.07	disky
SL2SJ085540-014730	0.365	3.48	5.21	222 ± 19	11.11 ± 0.10	2.15 ± 0.11	
SL2SJ090407-005952	0.611	16.81	9.47	178 ± 20	11.55 ± 0.12	1.48 ± 0.11	
SL2SJ095921+020638	0.552	3.47	4.73	195 ± 22	11.28 ± 0.11	2.12 ± 0.16	
SL2SJ135949+553550	0.783	13.08	8.52	229 ± 19	11.41 ± 0.15	1.86 ± 0.14	
SL2SJ140454+520024	0.456	11.78	14.80	337 ± 19	12.10 ± 0.10	1.95 ± 0.06	
SL2SJ140546+524311	0.526	4.58	9.48	291 ± 21	11.67 ± 0.11	2.14 ± 0.08	
SL2SJ140650+522619	0.716	4.35	6.79	258 ± 14	11.60 ± 0.15	2.01 ± 0.07	
SL2SJ141137+565119	0.322	3.04	4.34	220 ± 23	11.28 ± 0.09	2.15 ± 0.15	
SL2SJ142059+563007	0.483	7.86	8.39	228 ± 19	11.76 ± 0.10	1.93 ± 0.11	
SL2SJ220329+020518	0.400	3.86	10.49	218 ± 21	11.26 ± 0.10	1.77 ± 0.09	
SL2SJ220506+014703	0.476	3.93	9.87	326 ± 30	11.51 ± 0.10	2.19 ± 0.09	
SL2SJ221326-000946	0.338	2.41	5.17	177 ± 15	10.99 ± 0.10	1.89 ± 0.09	disky
SL2SJ222148+011542	0.325	5.27	6.59	224 ± 23	11.55 ± 0.09	1.96 ± 0.13	

Note. — Summary of lensing and dynamics measurements.

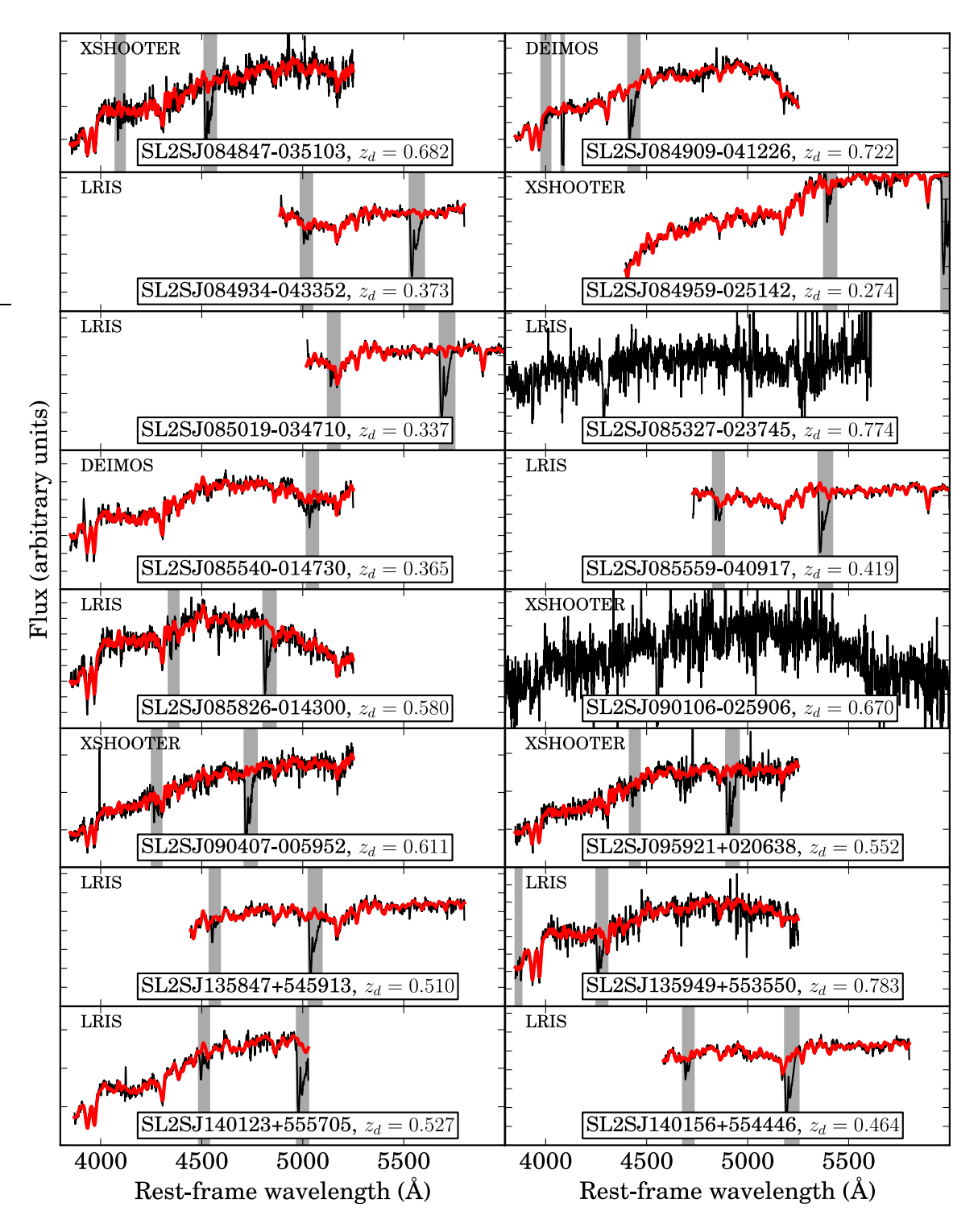


Fig. 1.— continued.

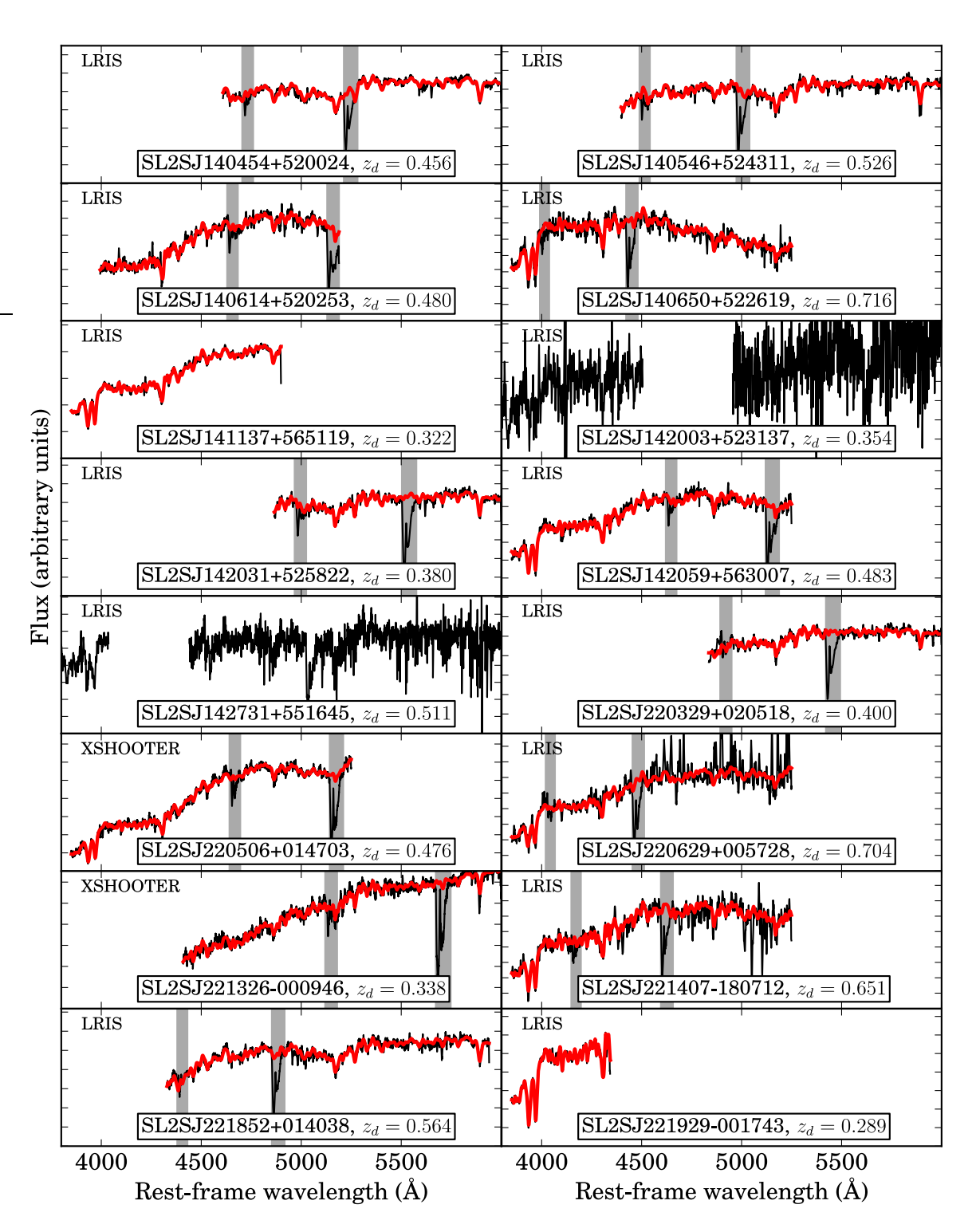


Fig. 1.— continued.

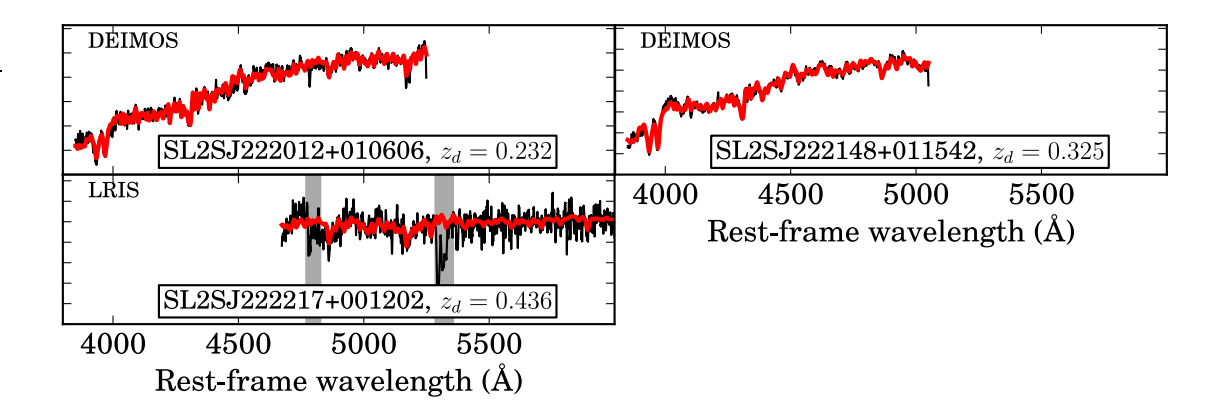


Fig. 1.— continued.

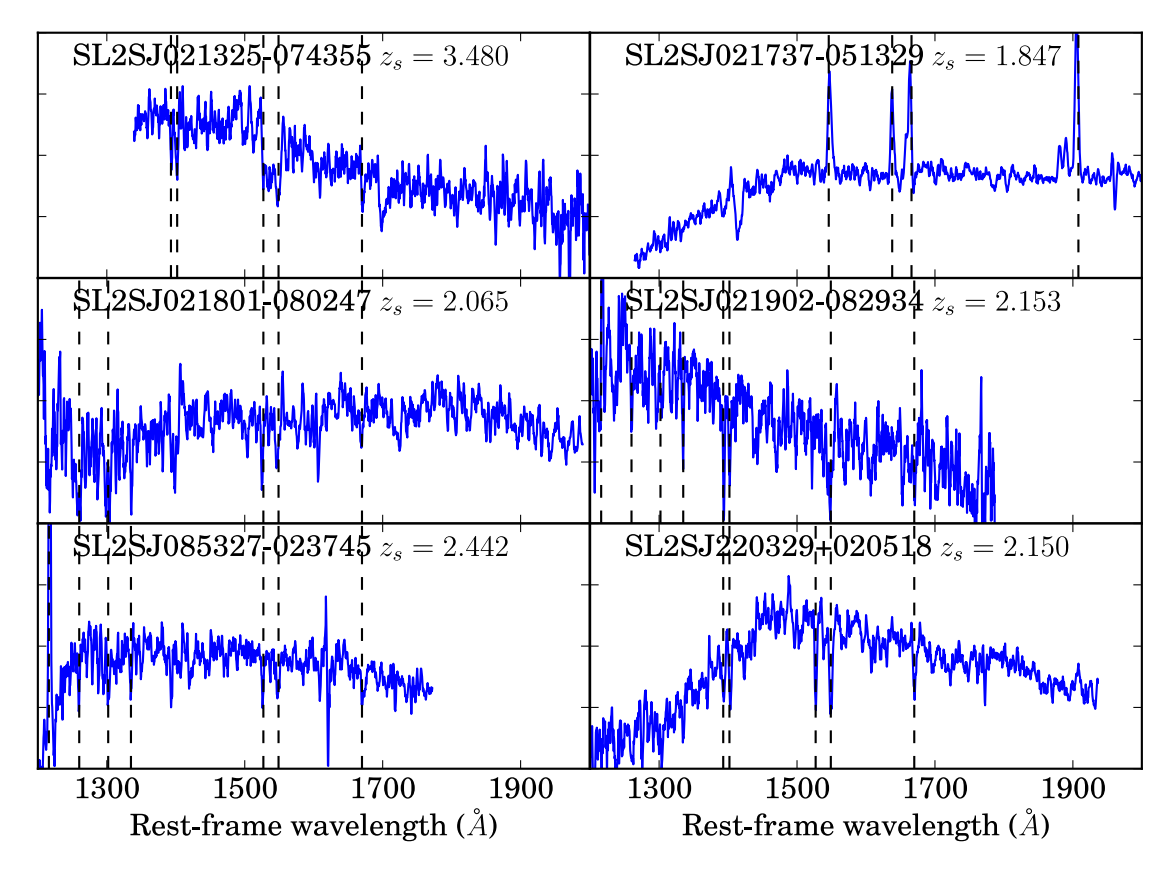


Fig. 2.— Spectra of lensed sources that are bright enough to be detected in the continuum. The vertical dashed lines highlight absorption/emission line features: in order of increasing wavelength Ly- α (1216Å), SiII (1260Å), SiII (1302Å, 1304Å), CII (1335Å), SiIV (1393Å, 1402Å), SiII (1527Å), CIV (1549Å), AlII (1670Å).

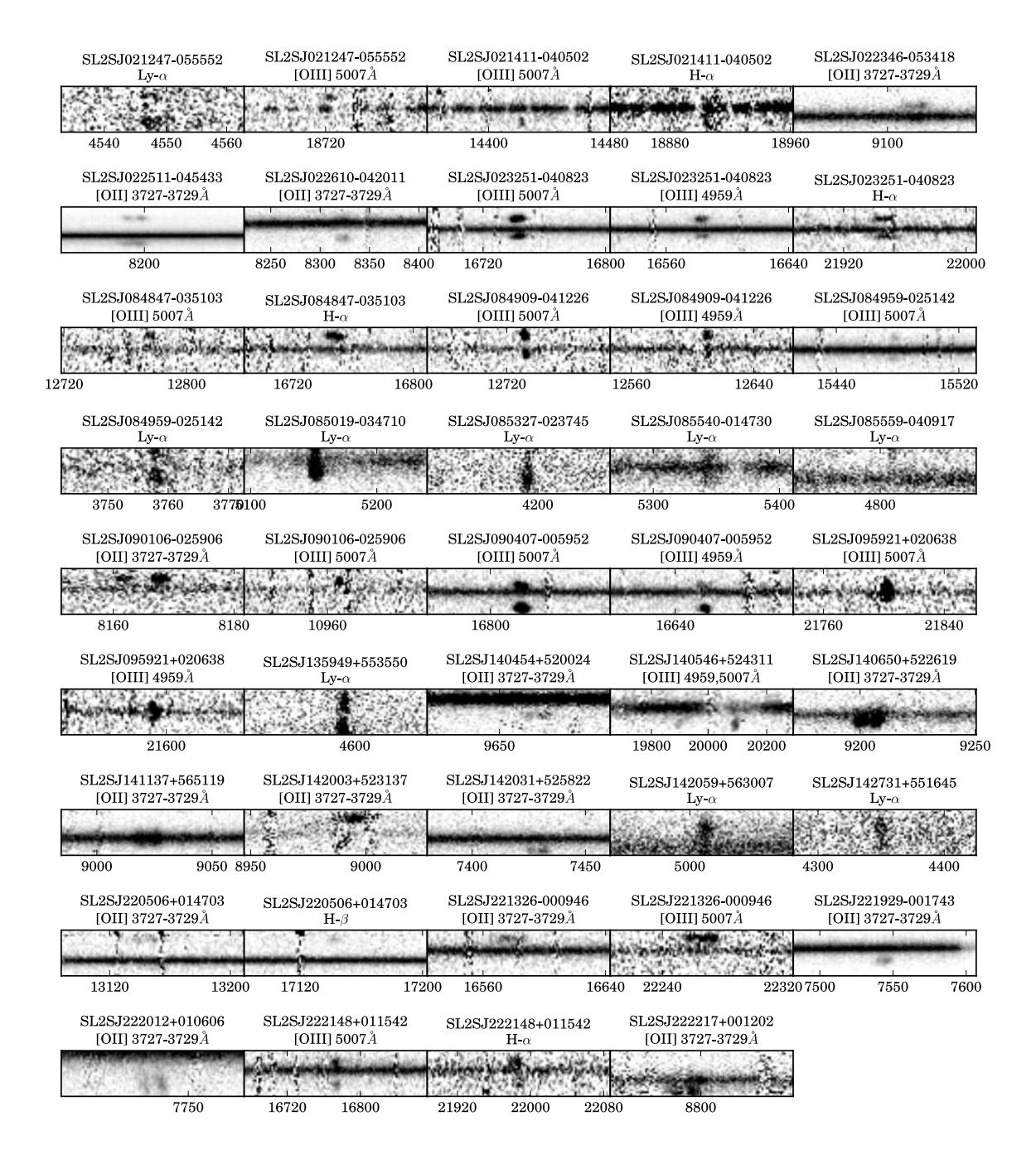


Fig. 3.— 2d spectra of SL2S lenses around the identified emission lines from the lensed arcs. Observer frame wavelength in Åis labeled on the horizontal axis.

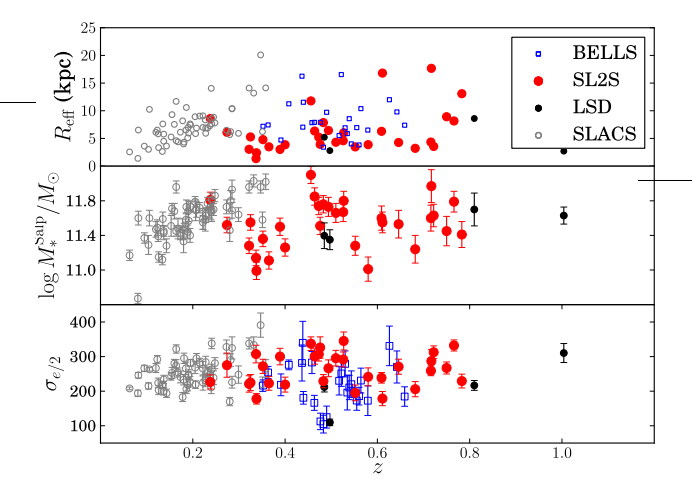


Fig. 4.— Effective radius, stellar mass and velocity dispersion of lenses as a function of redshift.

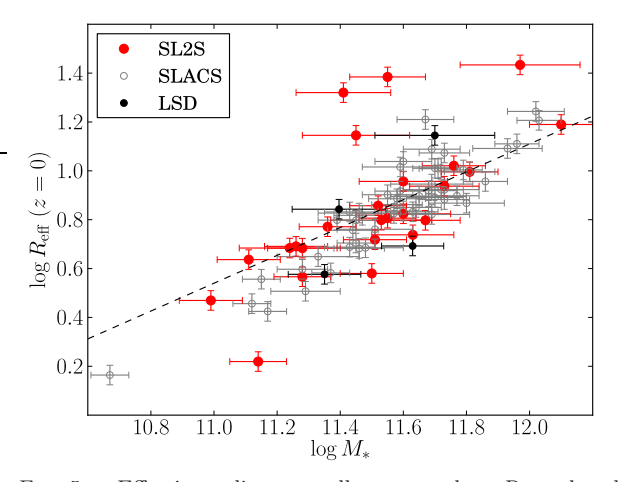


Fig. 5.— Effective radius vs. stellar mass, where $R_{\rm eff}$ values have been corrected for the evolution in the mass-size relation measured by Newman et al. (2012): $\log R_{\rm eff}(z=0) = \log R_{\rm eff} + 0.26z$. The dashed line indicates the mass-radius relation for SDSS galaxies measured by Newman et al. (2012).

However we would like to be more quantitative and explore the two following questions: what kind of average over the true density profile $\rho(r)$ best reproduces the lensing+dynamics γ' ? How sensitive to the ratio $R_{\rm Ein}/R_{\rm eff}$ is the measured γ' for a fixed galaxy mass profile? The former issue is relevant when comparing theoretical models to lensing and dynamics measurements. The latter is important when trying to measure trends of γ' with redshift: the ratio $R_{\rm Ein}/R_{\rm eff}$ typically increases for purely geometrical reasons, and a dependence of γ' on $R_{\rm Ein}/R_{\rm eff}$ could in principle bias the inference on the evolution of the slope. In order to answer these questions we simulate γ' measurements on a broad range of model mass profiles and compare these with the true density slopes. We consider a pure de Vaucouleurs profile, a sum of a de Vaucouleurs profile with a Navarro, Frenk & White (Navarro et al. 1997) profile with two values of the dark matter mass fraction $f_{\rm DM}$ within the 3d effective radius, and the most probable total density profile from the bulge + halo decomposition of the gravitational lens SDSSJ0946+1006 by Sonnenfeld et al. (2012). None

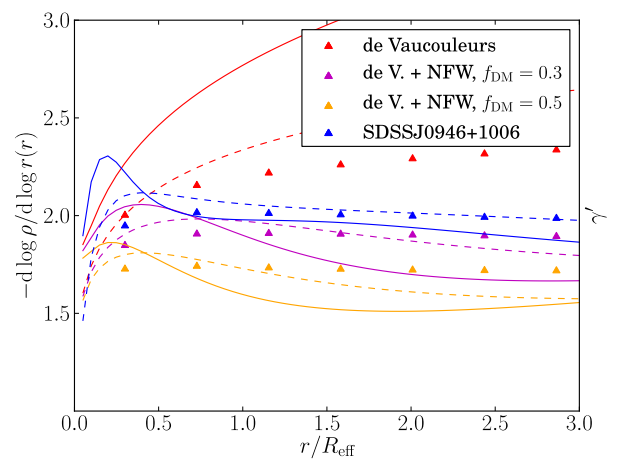


Fig. 6.— Solid lines: Local logarithmic density slope as a function of 3d radius, in units of the effective radius. Dashed lines: mass-weighted density slope within radius r. Triangles: lensing+dynamics γ' for $R_{\rm Ein}=r.$ Different colors indicate the different model mass profiles listed in the body text.

of these model profiles is a pure power law. We emphasize that the range of models is chosen to be broader than what is likely to be found in real galaxies based on the detailed analysis of SLACS systems by Barnabè et al. (2011).

We again use the spherical Jeans equation to calculate the central velocity dispersion for each of these model galaxies and then fit power law density profiles with fixed total projected mass within different Einstein radii. These simulated measurements of γ' are plotted in Figure 6 as a function of $R_{\rm Ein}/R_{\rm eff}$ for each model profile. In the same plot we show the local logarithmic density slope $-{\rm d}\log\rho/{\rm d}\log r$ as a function of r, and also the mass-weighted density slope within radius r

$$\langle \gamma'(r) \rangle_M = \frac{1}{M(r)} \int_0^r \gamma'(r') 4\pi r^2 \rho(r') dr',$$
 (1)

which has been suggested by Dutton & Treu (2013) to be a good proxy for the lensing + dynamics γ' .

Figure 6 shows that measurements of γ' (triangles) are remarkably independent of the ratio of the Einstein radius to the effective radius, for all models. This is an important result: it means that the physical interpretation of γ' measurements will be stable against different lenses having different values of $R_{\rm Ein}/R_{\rm eff}$. Excluding the pure de Vaucouleurs model, which is ruled out on many grounds (mass-follows light models fail to reproduce lensing and dynamical data, for example Koopmans & Treu 2003), the difference between the mass-weighted slope and the lensing and dynamics slope is generally smaller than the typical measurement errors on γ' of ~ 0.1 , particularly in the region $0.5R_{\rm eff} < r < R_{\rm eff}$. However the radius at which γ' and the mass-weighted slope are closest is slightly different for different mass profiles, and so it is difficult to interpret γ' precisely in terms of a massweighted slope within a fixed radius. For very accurate comparisons with lensing and dynamical data, we recommend simulating a lensing and dynamics measurement of the models.

6. DEPENDENCE OF THE MASS DENSITY PROFILE SLOPE γ' ON REDSHIFT, STELLAR MASS, AND EFFECTIVE RADIUS

The main goal of this work is to establish whether, and to what extent, γ' varies with redshift across the population of ETGs. It is useful to first study the trends of γ' on basic parameters (Section 6.1) in order to gain insights about the ingredients that will have to be considered in Section 6.2 to carry out a rigorous statistical analysis.

6.1. Qualitative exploration of the dependency of γ' on other parameters

Figure 7 shows the individual lens γ' values as a function of z for SL2S galaxies, as well as lenses from the SLACS (Auger et al. 2010a) and LSD (Treu & Koopmans 2004) surveys. A trend of γ' with z is clearly visible, with lower redshift objects having a systematically steeper slope than higher redshift ones, as previously found by Ruff et al. (2011) and Bolton et al. (2012). Before making more quantitative statements on the time evolution of γ' we would like to check whether the density slope correlates with quantities other than redshift. Galaxies grow in mass and size during their evolution, and a variation of γ' with time might be the result of a more fundamental dependence of the slope on structural properties of ETGs. Dependences of γ' on the effective radius and the stellar velocity dispersion were explored by Auger et al. (2010a), finding an anticorrelation with the former and no significant correlation with the latter. Here we consider the stellar mass, plotted against γ' in Figure 8. A weak trend is visible, with more massive galaxies having a shallower slope. However the stellar mass is a rather steep function of redshift in our sample (see Figure 4) and the trend seen in Figure 8 might just be the result of this selection function. In fact, if we fit for a linear dependence of γ' on both z and M_* we find that our data are consistent with γ' being independent of M_* at fixed z.

A quantity that is expected to correlate with γ' is the stellar mass density, $\Sigma_* = M_*/(2\pi R_{\rm eff}^2)$: galaxies with a more concentrated stellar distribution should have a steeper overall density profile. This was pointed out by Auger et al. (2010a) and Dutton & Treu (2013) and is seen in our data, as shown in Figure 9. It is therefore important to account for a dependence of γ' on Σ_* , or on the two independent variables on which this quantity depends, $R_{\rm eff}$ and M_* , when fitting for the time dependence of the density slope. This is done in the next Section.

6.2. Quantitative Inference

In this Section we aim to quantify how the mean density slope $\langle \gamma' \rangle$ depends on galaxy properties, and on lookback time. The population of ETGs is known to be well-described by two parameters, as revealed by the existence of the Fundamental Plane relation (Djorgovski & Davis 1987; Dressler et al. 1987). Two parameters are then probably sufficient to capture the variation of γ' across the population of ETGs. For our analysis we focus on stellar mass and effective radius (this includes also dependencies on stellar mass density, which is believed to be an important parameter driving γ' , as discussed above). Our objective is then to measure the trends in γ' across the three-dimensional space defined by $(z, M_*, R_{\rm eff})$. This is done with a simple but rigorous

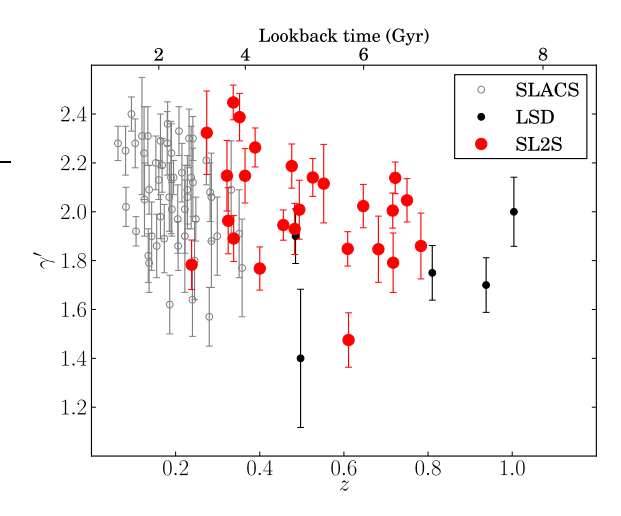
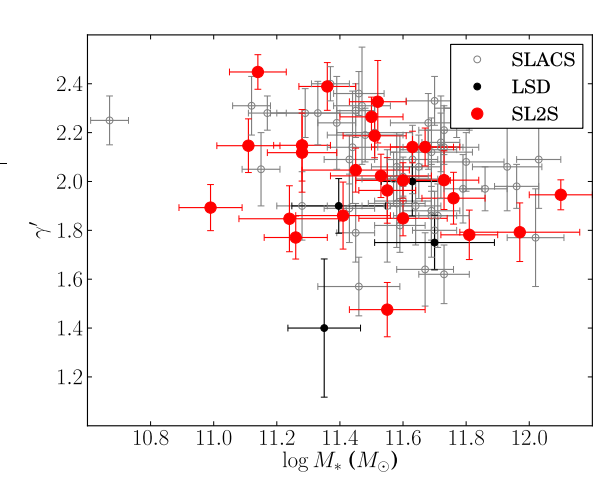


Fig. 7.— Density slope as a function of redshift for SL2S, SLACS and LSD galaxies.



 ${\it Fig.~8.--}$ Density slope as a function of stellar mass. A Salpeter IMF is assumed.

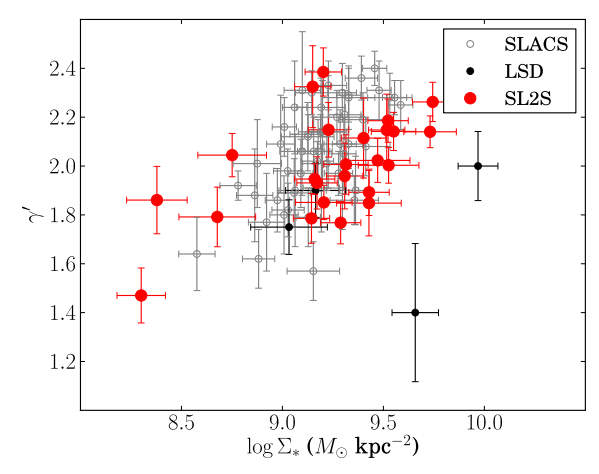


Fig. 9.— Density slope as a function of stellar mass density.

Bayesian inference method. We assume that the values of the slope γ' of our lenses are drawn from a Gaussian distribution with mean given by

$$\langle \gamma' \rangle = \gamma'_0 + \alpha(z - 0.3) + \beta(\log M_* - 11.5) + \xi \log(R_{\text{eff}}/5)$$
(2)

and dispersion $\sigma_{\gamma'}$. The stellar mass is in solar units and the effective radius in kpc. We also assume that individual stellar masses $M_{*,i}$ are drawn from a parent distribution that we approximate as a Gaussian:

$$\Pr(M_{*,i}) = \frac{1}{\sigma_{M_*} \sqrt{2\pi}} \exp\left[-\frac{\left(\log M_{*,i} - \mu_{M_*}^{(\text{Samp})}(z_i)\right)}{2\sigma_{M_*}^{2(\text{Samp})}}\right].$$
(3)

To account for selection effects, we allow for a different mean stellar mass and dispersion for lenses of different surveys. We also let the mean stellar mass be a function of redshift. This choice reflects the clear trend of stellar mass with redshift seen in Figure 4 for both the SLACS and the SL2S samples, which in turn is determined by SLACS and SL2S both being magnitude-limited samples. The parameter describing the mean stellar mass is then

$$\mu_{M_*}^{(\text{SLACS})} = \zeta^{(\text{SLACS})}(z_i - 0.2) + \log M_{*,0}^{(\text{SLACS})}$$
 (4)

for SLACS galaxies and

$$\mu_{M_*}^{(\text{SL2S})} = \zeta^{(\text{SL2S})}(z_i - 0.5) + \log M_{*,0}^{(\text{SL2S})}$$
 (5)

for SL2S and LSD galaxies. We assume flat priors on all the model parameters and fit for them with a Markov chain Monte Carlo following Kelly (2007). The stellar masses considered in this model are those measured in Paper III assuming a Salpeter IMF. The full posterior probability distribution function is shown in Figure 10 and the median, 16th and 84th percentile of the probability distribution for the individual parameters, obtained by marginalizing over the remaining parameters, is given in Table 4. The fit is done first with SL2S galaxies only and then repeated by adding SLACS and LSD lenses. For six lenses of the SLACS sample Auger et al. (2010a) warn that their velocity dispersions might be significantly incorrect, and we conservatively exclude them from our fit. These are SSDSJ0029-0055, SDSSJ0737+3216, SDSSJ0819+4534, SDSSJ0935-0003, SDSSJ1213+6708 and SDSSJ1614+4522.

By using only the 25 SL2S lenses for which γ' measurements are possible, we are able to detect a trend of $\langle \gamma' \rangle$ with R_{eff} at the 3-sigma level and a dependence on M_* at the 1-sigma level: at fixed z and M_* , galaxies with a smaller effective radius have a steeper density profile. Similarly, at fixed $R_{\rm eff}$, galaxies with a larger stellar mass have a marginally larger γ' . If we add 53 lenses from SLACS and 4 lenses from the LSD survey, the trends with M_* and R_{eff} are confirmed at a higher significance, and we detect a dependence of $\langle \gamma' \rangle$ on redshift at the 3-sigma level. Lower redshift objects appear to have a steeper slope than higher redshift counterparts at fixed mass and size. Incidentally, the median value of ξ , the parameter describing the linear dependence of $\langle \gamma' \rangle$ on $\log R_{\text{eff}}$, is nearly -2 times β , the parameter describing the dependence on $\log M_*$. This suggests that $\langle \gamma' \rangle$ grows roughly as $\beta \log (M_*/R_{\rm eff}^2)$, which is equivalent to the stellar mass density. It appears then that

the dependence of γ' on the structure of ETGs can be well summarized with a dependence on stellar mass density, leaving little dependence on M_* or $R_{\rm eff}$ individually. This confirms and extends the trend with surface mass density seen by Auger et al. (2010a) and Dutton & Treu (2013).

We then repeated the fit allowing only for a dependence of $\langle \gamma' \rangle$ on redshift and stellar mass density:

$$\langle \gamma' \rangle = \gamma_0 + \alpha(z - 0.3) + \eta(\log \Sigma_* - 9.0). \tag{6}$$

This model has one less free parameter with respect to Equation 2. Our inference on the parameter describing the dependence on Σ_* is $\eta = 0.38 \pm 0.07$, and the scatter in γ' is $\sigma_{\gamma'} = 0.12 \pm 0.02$, the same value measured for the more general model of Equation 2. This is again suggesting that the dependence of γ' on the stellar mass density might be of a more fundamental nature than dependences on mass and size separately.

7. DISCUSSION

The main result of the previous section is that the ensemble average total mass density slope of galaxies of a fixed stellar mass increases with cosmic time (i.e. decreases with redshift). This trend with redshift is detected at the $3-\sigma$ confidence level and is in good agreement with previous results from Ruff et al. (2011) and Bolton et al. (2012).

Before discussing the physical interpretation of this result, however, it is important to emphasize that what we are measuring is how the population mean density slope changes in the $(z, M_*, R_{\rm eff})$ space within the population of early-type galaxies, and not how γ' changes along the lifetime of an individual galaxy, $\mathrm{d}\gamma'/\mathrm{d}z$. In order to infer the latter quantity we need to evaluate the variation of γ' along the evolutionary track of the galaxy as this moves in the $(z, M_*, R_{\rm eff})$ space. This requires to know how both mass and size of the galaxy change with time, since the slope depends on these parameters. More formally,

$$\frac{\mathrm{d}\gamma'(z, \log M_*, \log R_{\mathrm{eff}})}{\mathrm{d}z} = \frac{\partial\gamma'}{\partial z} + \frac{\partial\gamma'}{\partial \log M_*} \frac{\mathrm{d}\log M_*}{\mathrm{d}z} + \frac{\partial\gamma'}{\partial \log R_{\mathrm{eff}}} \frac{\mathrm{d}\log R_{\mathrm{eff}}}{\mathrm{d}z}.$$
(7)

In a parallel with fluid mechanics, our description of the population of galaxies of Section 5 is Eulerian, while Equation 7 is a Lagrangian specification of the change in time of the mean slope of an individual galaxy, providing a more straightforward way to physically understand the evolution of ETGs.

With all these terms entering Equation 7, it is no longer clear if the density slope is indeed getting steeper with time for individual objects. In particular, we have observed that γ' depends significantly on stellar mass density (and thus effective radius). It is then crucial to consider all the terms of the equation before reaching a conclusion. Fortunately this can be done by combining our measurements with results from the literature.

In the context of our model specified in Equation 2, the partial derivatives introduced above can be identified and evaluated as follows:

$$\frac{\partial \gamma'}{\partial z} = \alpha = -0.31 \pm 0.10,\tag{8}$$

$$\gamma' = \gamma_0 + \alpha(z - 0.3) + \beta(\log M_* - 11.5) + \xi(\log \Sigma_* - 9.0) + N(0, \sigma_{\gamma'})$$

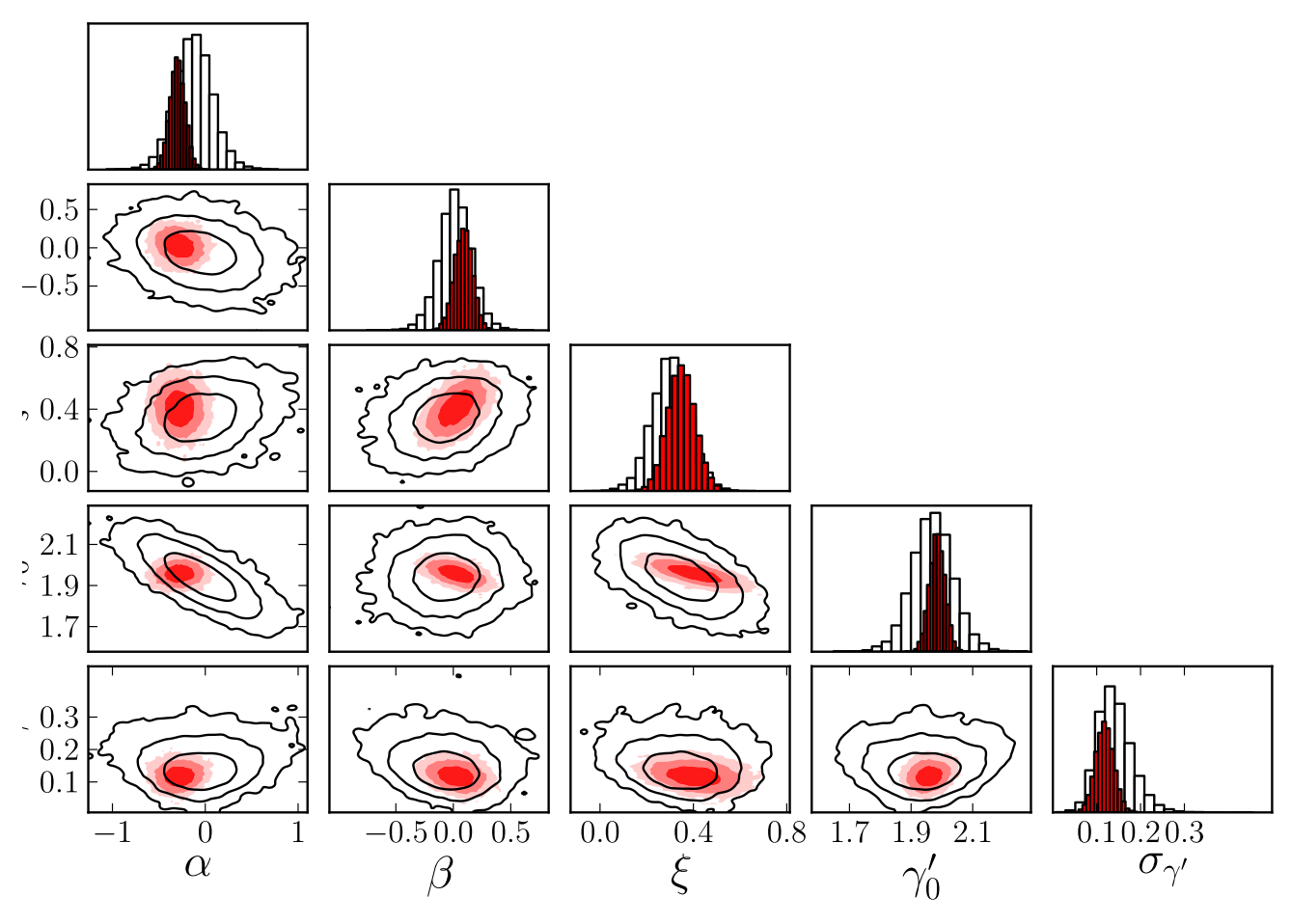


Fig. 10.— Posterior probability distribution function for the model parameters of equation (2). Empty contours: Inference with SL2S galaxies only. Filled contours: SL2S + SLACS + LSD lenses. The different levels represent the 68%, 95% and 99.7% enclosed probability regions.

TABLE 4 LINEAR MODEL WITH SCATTER.

$\begin{array}{cccccccccccccccccccccccccccccccccccc$	Parameter	SL2S only	SL2S + SLACS + LSD	Notes
$ \xi = \begin{array}{ccccccccccccccccccccccccccccccccccc$	$\begin{array}{c} \zeta^{(\mathrm{SL2S})} \\ \sigma^{(\mathrm{SL2S})} \\ \log M_{*,0}(\mathrm{SLACS}) \\ \zeta^{(\mathrm{SLACS})} \\ \sigma^{(\mathrm{SLACS})} \\ \sigma^{(\mathrm{SLACS})} \\ \alpha \\ \beta \\ \xi \\ \gamma_0 \end{array}$	$0.25^{+0.05}_{-0.04}\\ \dots\\ -0.13^{+0.24}_{-0.24}\\ 0.31^{+0.23}_{-0.23}\\ -0.67^{+0.20}_{-0.20}\\ 2.05^{+0.06}_{-0.06}$	$\begin{array}{c} 0.23^{+0.04}_{-0.04} \\ 11.59^{+0.03}_{-0.03} \\ 2.35^{+0.39}_{-0.39} \\ 0.17^{+0.02}_{-0.02} \\ -0.31^{+0.09}_{-0.16} \\ 0.40^{+0.16}_{-0.15} \\ -0.76^{+0.15}_{-0.15} \\ 2.08^{+0.02}_{-0.02} \end{array}$	Linear dependence of mean stellar mass on redshift, SL2S sample Scatter in mean stellar mass, SL2S sample Mean stellar mass at $z=0.2$, SLACS sample Linear dependence of mean stellar mass on redshift, SLACS sample Scatter in mean stellar mass, SLACS sample Linear dependence of γ' on redshift. Linear dependence of γ' on $\log M_*$. Linear dependence of γ' on $\log R_{\rm eff}$. Mean slope at $z=0.3$, $\log M_*=11.5$, $R_{\rm eff}=5$ kpc

$$\frac{\partial \gamma'}{\partial \log M_*} = \beta = 0.40 \pm 0.16,\tag{9}$$

$$\frac{\partial \gamma'}{\partial \log R_{\text{eff}}} = \xi = -0.76 \pm 0.15. \tag{10}$$

Note that we are not considering the effects of scatter: we are assuming that the change in γ' is the same as that of a galaxy that evolves while staying at the mean γ' as it moves through the (z, M_*, R_{eff}) space. By doing so, the evolution in the slope that we derive from Equation 7 will be representative of the mean change in γ' over the population, while individual objects can have different evolutionary tracks, within the limits allowed by our constraints on $\sigma_{\gamma'}$.

The remaining quantities to be estimated are the rate of mass and size growth. In the hierarchical merging picture ETGs are expected to grow in stellar mass with time, therefore $\mathrm{d}M_*/\mathrm{d}z < 0$. Observationally, we know massive early-type galaxies grow at most by a factor of two in stellar mass since z=1 (see, e.g., Lin et al. 2013, and references therein). Thus we can conservatively take the mean between zero and 2, even though we will show below that our conclusion are virtually insensitive to this choice:

$$\frac{\mathrm{d}\log M_*}{\mathrm{d}z} = -0.15 \pm 0.15. \tag{11}$$

The effective radius grows as a result of the growth in mass, but is itself an evolving quantity at fixed M_* (Damjanov et al. 2011; Newman et al. 2012; Cimatti et al. 2012; Poggianti et al. 2013): $R_{\rm eff} = R_{\rm eff}(z, M_*(z))$. We assume that ETGs grow while staying on the observed $M_* - R_{\rm eff}$ relation at all times. Then we can write

$$\frac{\mathrm{d} \log R_{\mathrm{eff}}}{\mathrm{d}z} = \frac{\partial \log R_{\mathrm{eff}}}{\partial z} + \frac{\partial \log R_{\mathrm{eff}}}{\partial \log M_*} \frac{\mathrm{d} \log M_*}{\mathrm{d}z}$$
(12)

and use the values measured by Newman et al. (2012), $\partial \log R_{\rm eff}/\partial z = -0.26 \pm 0.02$ and $\partial \log R_{\rm eff}/\partial \log M_* = 0.59 \pm 0.07$.

Plugging these values into Equation 7 we find that

$$\frac{\mathrm{d}\gamma'}{\mathrm{d}z} = (-0.31 \pm 0.10) + (0.40 \pm 0.15)(-0.15 \pm 0.15) + (-0.76 \pm 0.15)[(-0.26 \pm 0.02) + (-0.15 \pm 0.15)(0.59 \pm 0.07)] = -0.10 \pm 0.12$$
(13)

Note that $\mathrm{d}\gamma'/\mathrm{d}z$ has little dependence on the mass growth rate $\mathrm{d}\log M_*/\mathrm{d}z$, which is the most poorly known quantity in this model. To be more quantitative we plot in Figure 11 the total derivative $\mathrm{d}\gamma'/\mathrm{d}z$ as a function of $\mathrm{d}\log M_*/\mathrm{d}z$, and show that for any plausible value, spanning over an order of magnitude, the answer is unchanged. Different assumptions on the evolution of the size-mass relation do not change significantly our result. For instance, Damjanov et al. (2011) find a more rapid evolution of R_{eff} than Newman et al. (2012), leading to $\mathrm{d}\gamma'/\mathrm{d}z = 0.06 \pm 0.15$, consistent with no change of the total mass density profile with time.

Thus, the key result is that, when considering all the terms of Equation 7, we find that, on average, individual ETGs grow at approximately constant density slope.

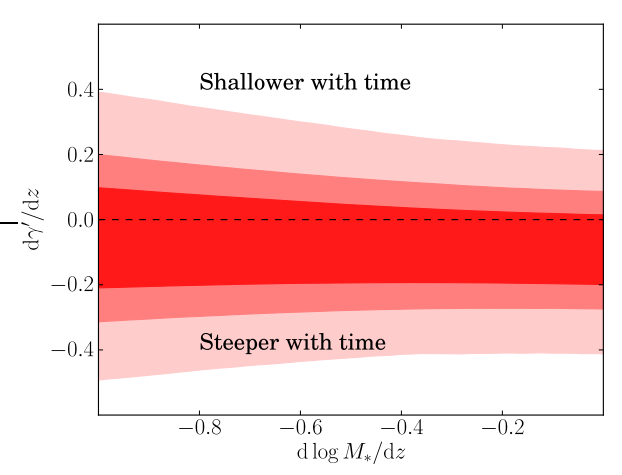


Fig. 11.— Mean intrinsic change of the density slope with redshift of a massive ETG, as a function of its mass growth rate.

The observed redshift dependence of γ' at fixed mass and size can then be understood as the result of the evolution of the size-mass relation and by the dependency of γ' on the stellar mass density. Qualitatively, in this picture an individual galaxy grows in stellar mass and size so as to decrease its central stellar mass density. During this process, the slope of its total mass density profile does not vary significantly. However the other galaxies that now find themselves to have the original stellar mass and effective radius of this galaxy had originally a steeper mass density profile, thus giving rise to the observed trend in $\partial \gamma'/\partial z$.

This is illustrated in Figure 12, where we show a possible scenario consistent with the observations. The evolutionary tracks of two representative galaxies between z = 1 and z = 0 are shown as solid black arrows, in the multi-dimensional parameter space of stellar mass, effective radius, effective density, and slope of the mass density profile γ' . The two galaxies are chosen so that one has at z = 1 the same mass and effective radius that the other has at z = 0. Mass and size are evolved following Equation 11 and Equation 12. We then assign γ' at z=0 based on the observed correlation with size and stellar mass (effectively with effective stellar mass density, since $\beta \approx -2\xi$) and assume it does not evolve for an individual galaxy. The apparent evolution of γ' at fixed M_* and $R_{\rm eff}$ is consistent with the measured value $\partial \gamma'/\partial z = -0.31 \pm 0.10$, and is dictated by a difference in the initial stellar density of their progenitors, being larger for the more massive object.

In the context of simple one-parameter stellar profiles (e.g. de Vaucouleurs), this difference in γ' at fixed mass and size for galaxies at different redshift must be ascribed to corresponding differences in the underlying dark matter distribution. The implications of our results for the dark matter profiles of ETGs will be explored in an upcoming paper (Sonnenfeld et al., in prep.).

An important assumption at the basis of our analysis is that scaling relations of γ' with mass and size measured at low redshift can be used to predict the evolution of the slope for higher redshift objects. This assumption holds well if the evolutionary tracks of higher redshift galaxies stay on parts of the parameter space probed by the lower redshift systems. To first approximation this seems to

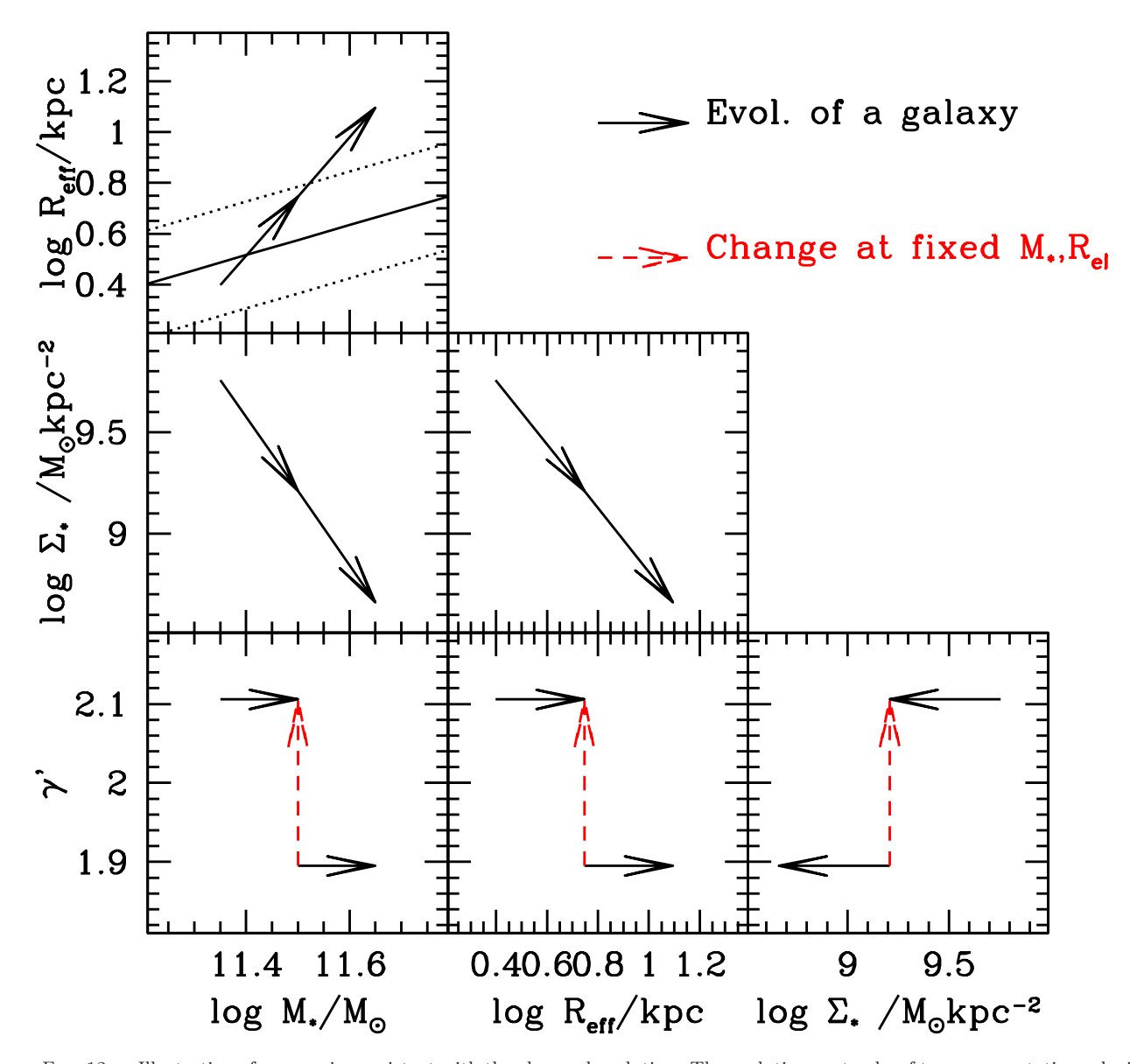


Fig. 12.— Illustration of a scenario consistent with the observed evolution. The evolutionary tracks of two representative galaxies between z=1 and z=0 are shown as solid black arrows, in the multidimensional parameter space of stellar mass, effective radius, effective density, and slope of the mass density profile γ' . Measured correlations with stellar mass are used to assign the other parameters as described in the text. The solid and dotted lines in the top left panel show the mass-size relation at z=1 from Newman et al. (2012) and the scatter around it. Even if γ' is assumed not to change for an individual galaxy, γ' at fixed stellar mass and size is observed to increase reflecting the difference in their initial (z=1) stellar density, as shown by the red dashed arrows.

be the case for the galaxies in our sample. Figure 5 shows the positions of our lenses in the $M_*-R_{\rm eff}$ space, where the effective radius of each object is renormalized by the average $R_{\rm eff}$ of galaxies at its redshift. Under our assumptions, objects evolve along lines parallel to the mass-size relation (dashed line) towards higher masses. There is significant overlap between the high-z SL2S-LSD sample and the lower redshift SLACS sample, implying that SLACS galaxies are informative on the evolution in γ' of SL2S-LSD objects. Differently, one could rely on extrapolations of the scaling relations for γ' .

A more quantitative explanation of our findings would require a detailed comparison with theoretical model and is beyond the scope of this work. However, we can check at least qualitatively how our result compares with published predictions. Nipoti et al. (2009b) studied the impact of dissipationless (dry) mergers on γ' finding that for an individual galaxy the slope tends to get shallower with time. Johansson et al. (2012) looked at the evolution in the slope on nine ETGs in cosmological simulations, finding no clear trend in the redshift range explored by our data. Their simulations include both dry and dissipational (wet) mergers. Remus et al. (2013) examined simulated ETGs in a cosmological framework and in binary mergers. They found slopes that become shallower in time, asymptotically approaching the value $\gamma'\approx 2.1$ as observed in our data. They also detected a correlation between the amount of in-situ star formation and slope,

with γ' being larger in systems that experienced more star formation events. Finally, Dubois et al. (2013) produced zoomed cosmological simulations of ETGs with or without AGN feedback. They found that the total density slope becomes steeper with time. They also observed that galaxies with strong AGN feedback have a shallower profile than systems with no AGN feedback and interpreted this result with the AGN shutting off in-situ star formation. Qualitatively, our data is not in stark contrast with any of these models.

A more quantitative comparison is required to find out whether the models work in detail. This is left for future work. The combination of constraints from the evolution of the size stellar mass relation obtained via traditional studies of large samples of ETGs, and our own detailed measurements of the evolution of their internal structure should provide a stringent test for evolutionary models of ETGs, and thus help us improve our understanding of the baryonic and dark matter physics relevant at kpc scales.

8. SUMMARY AND CONCLUSIONS

We have presented spectroscopic observations from the Keck, VLT, and Gemini Telescopes of a sample of 53 lenses and lens candidates from the SL2S survey. We measured stellar velocity dispersions for 47 of them, and redshifts of both lens and background source for 35 of them. 36 systems are confirmed grade A lenses and 25 of these were able to be used for a lensing and stellar dynamics analysis. We have shown how spectroscopic observations can be used in combination with ground-based imaging with good seeing ($\sim 0.7''$) to confirm gravitational lens candidates by the presence of multiply imaged emission lines from the lensed background source. We have also shown how SL2S lenses are comparable with lenses from other surveys in terms of their size, mass and velocity dispersion, and lie on the same $M_* - R_{\text{eff}}$ relation as non-lens galaxies.

By fitting a power-law density profile $(\rho(r) \propto r^{-\gamma'})$ to the lensing and stellar kinematics data of SL2S, SLACS and LSD lenses we measured the dependence of γ' on redshift, stellar mass and galaxy size, over the ranges $z \approx 0.1-1.0$, $\log M_*/M_{\odot} \approx 11-12$, $R_{\rm eff} = 1-20 {\rm kpc}$.

Our main results can be summarized as follows:

- 1. In the context of power-law models for the density profile $\rho_{\text{tot}} \propto r^{-\gamma'}$, the (logarithmic) density slope γ' of the SL2S lenses is approximately but not exactly that of a single isothermal sphere ($\gamma' = 2$), consistent with previous studies of lenses in different samples. This can be understood as the result of the combination of a stellar mass density profile that falls off more steeply than the dark matter halo. The relative scaling of the two conspires to produce the power law index close to isothermal ("bulge-halo" conspiracy).
- 2. At a given redshift, the mass density slope γ' depends on the surface stellar mass density $\Sigma_* = M_*/2R_{\rm eff}^2$, in the sense that galaxies with denser stars also have steeper total mass density profiles $(\partial \gamma'/\partial \log \Sigma_* = 0.38 \pm 0.07)$.
- 3. At fixed M_* and R_{eff} , $\langle \gamma' \rangle$ depends on redshift, in the sense that galaxies at a lower redshifts have on

- average a steeper average slope $(\partial \gamma'/\partial z = -0.31 \pm 0.10)$.
- 4. Once the dependencies of γ' on redshift and surface stellar mass density are taken into account, less than 6% intrinsic scatter is left ($\sigma'_{\gamma} = 0.12 \pm 0.02$).
- 5. The average redshift evolution of γ' for an individual galaxy is consistent with zero: $\mathrm{d}\gamma'/\mathrm{d}z = -0.10 \pm 0.12$. This result is obtained by combining our measured dependencies of $\langle \gamma' \rangle$ on redshift stellar mass and effective radius with the observed evolution of the size stellar mass relation taken from the literature.

The key result of this work is that the dependency of $\langle \gamma' \rangle$ on redshift and stellar mass density does not imply that massive early-type galaxies change their mass density profile over the second half of the lifetime. In fact, at least qualitatively, the observed dependencies can be understood as the results of two effects. Individual galaxies grow in stellar mass and decrease in density over the redshift range 1 to 0, while apparently largely preserving their total mass density profiles. This could be explained by the addition of stellar mass in the outer part of the galaxies in quantities that are sufficient to explain the decrease in stellar mass density but insufficient to alter the total mass density profile, since the regions are already dark matter dominated. As shown by Nipoti et al. (2012), the growth in size during this period is slow enough that it could perhaps be explained by the the infall of dark matter and stars via a drizzle of minor mergers, with material of decreasing density, tracking the decreasing cosmic density. This process needs to happen while substantially preserving the total mass density pro-

Alternatively, the evolution at constant slope can be interpreted as the combined effect of the decrease in stellar mass density and a variation in the dark matter profile (either a steepening or a decrease of the central dark matter distribution). The latter effect would be responsible for the term $\partial \gamma'/\partial z$.

Checking whether these scenarios can work quantitatively requires detailed comparisons with theoretical calculations, which are beyond the scope of this paper.

The second important result of this work is that the total mass density profile of early-type galaxies depends on their stellar mass density, with very little scatter. Qualitatively this makes sense, as we expect that the more concentrated stellar distributions should have been able to contract the overall profile the most. Presumably this difference may trace back to differences in past star formation efficiency or merger history. Therefore, the tightness of the observed correlation should provide interesting constraints on these crucial ingredients of our understanding of early-type galaxies.

We thank our friends of the SLACS and SL2S collaborations for many useful and insightful discussions over the course of the past years. We thank V.N. Bennert and M. Bradac for their help in our observational campaign. TT thanks S.W. Allen and B. Poggianti for useful discussions. RG acknowledges support from the Centre

National des Etudes Spatiales (CNES). PJM acknowledges support from the Royal Society in the form of a research fellowship. TT acknowledges support from the NSF through CAREER award NSF-0642621, and from the Packard Foundation through a Packard Research Fellowship. This research is based on XSHOOTER observations made with ESO Telescopes at the Paranal Observatory under programme IDs 086.B-0407(A) and 089.B-0057(A). This research is based on observations obtained with MegaPrime/MegaCam, a joint project of CFHT and CEA/DAPNIA, and with WIRCam, a joint project of CFHT, Taiwan, Korea, Canada and France, at the Canada-France-Hawaii Telescope (CFHT) which is operated by the National Research Council (NRC) of Canada, the Institut National des Sciences de l'Univers of the Centre National de la Recherche Scientifique (CNRS) of France, and the University of Hawaii. This work is based in part on data products produced at TERAPIX and the Canadian Astronomy Data Centre. The authors would like to thank S. Arnouts, L. Van waerbeke and G. Morrison for giving access to the WIRCam data collected

in W1 and W4 as part of additional CFHT programs. We are particularly thankful to Terapix for the data reduction of this dataset. This research is supported by NASA through Hubble Space Telescope programs GO-10876, GO-11289, GO-11588 and in part by the National Science Foundation under Grant No. PHY99-07949, and is based on observations made with the NASA/ESA Hubble Space Telescope and obtained at the Space Telescope Science Institute, which is operated by the Association of Universities for Research in Astronomy, Inc., under NASA contract NAS 5-26555, and at the W.M. Keck Observatory, which is operated as a scientific partnership among the California Institute of Technology, the University of California and the National Aeronautics and Space Administration. The Observatory was made possible by the generous financial support of the W.M. Keck Foundation. The authors wish to recognize and acknowledge the very significant cultural role and reverence that the summit of Mauna Kea has always had within the indigenous Hawaiian community. We are most fortunate to have the opportunity to conduct observations from this mountain.

REFERENCES

Atkinson, A. M., Abraham, R. G., & Ferguson, A. M. N. 2013, ApJ, 765, 28

Auger, M. W., Treu, T., Bolton, A. S., Gavazzi, R., Koopmans, L. V. E., Marshall, P. J., Moustakas, L. A., & Burles, S. 2010a, ApJ, 724, 511

Auger, M. W., Treu, T., Gavazzi, R., Bolton, A. S., Koopmans, L. V. E., & Marshall, P. J. 2010b, ApJ, 721, L163

Barnabè, M., Czoske, O., Koopmans, L. V. E., Treu, T., & Bolton, A. S. 2011, MNRAS, 415, 2215

Bolton, A. S., Brownstein, J. R., Kochanek, C. S., Shu, Y., Schlegel, D. J., Eisenstein, D. J., Wake, D. A., Connolly, N., Maraston, C., & Weaver, B. A. 2012, ArXiv e-prints

Bolton, A. S., Burles, S., Koopmans, L. V. E., Treu, T., Gavazzi, R., Moustakas, L. A., Wayth, R., & Schlegel, D. J. 2008, ApJ, submitted

Brewer, B. J., Dutton, A. A., Treu, T., Auger, M. W., Marshall, P. J., Barnabè, M., Bolton, A. S., Koo, D. C., & Koopmans, L. V. E. 2012, MNRAS, 422, 3574

Browne, I. W. A., et al. 2003, MNRAS, 341, 13

Brownstein, J. R., Bolton, A. S., Schlegel, D. J., Eisenstein, D. J., Kochanek, C. S., Connolly, N., Maraston, C., Pandey, P., Seitz, S., Wake, D. A., Wood-Vasey, W. M., Brinkmann, J., Schneider, D. P., & Weaver, B. A. 2012, ApJ, 744, 41

Cabanac, R. A., Alard, C., Dantel-Fort, M., Fort, B., Gavazzi, R., Gomez, P., Kneib, J. P., Le Fèvre, O., Mellier, Y., Pello, R., Soucail, G., Sygnet, J. F., & Valls-Gabaud, D. 2007, A&A, 461, 813

Cappellari, M., McDermid, R. M., Alatalo, K., Blitz, L., Bois, M., Bournaud, F., Bureau, M., Crocker, A. F., Davies, R. L., Davis, T. A., de Zeeuw, P. T., Duc, P.-A., Emsellem, E., Khochfar, S., Krajnović, D., Kuntschner, H., Morganti, R., Naab, T., Oosterloo, T., Sarzi, M., Scott, N., Serra, P., Weijmans, A.-M., & Young, L. M. 2013, MNRAS

Carollo, C. M., Bschorr, T. J., Renzini, A., Lilly, S. J., Capak, P., Cibinel, A., Ilbert, O., Onodera, M., Scoville, N., Cameron, E., Mobasher, B., Sanders, D., & Taniguchi, Y. 2013, ArXiv

Cimatti, A., Nipoti, C., & Cassata, P. 2012, MNRAS, 422, L62
Cooper, M. C., Newman, J. A., Davis, M., Finkbeiner, D. P., & Gerke, B. F. 2012, spec2d: DEEP2 DEIMOS Spectral Pipeline, astrophysics Source Code Library

Damjanov, I., Abraham, R. G., Glazebrook, K., McCarthy, P. J., Caris, E., Carlberg, R. G., Chen, H.-W., Crampton, D., Green, A. W., Jørgensen, I., Juneau, S., Le Borgne, D., Marzke, R. O., Mentuch, E., Murowinski, R., Roth, K., Savaglio, S., & Yan, H. 2011, ApJ, 739, L44 De Lucia, G., Springel, V., White, S. D. M., Croton, D., & Kauffmann, G. 2006, MNRAS, 366, 499 de Vaucouleurs, G. 1948, Annales d'Astrophysique, 11, 247

de Vaucouleurs, G. 1948, Annales d'Astrophysique, 11, 2 Djorgovski, S., & Davis, M. 1987, ApJ, 313, 59

Dressler, A., Lynden-Bell, D., Burstein, D., Davies, R. L., Faber, S. M., Terlevich, R., & Wegner, G. 1987, ApJ, 313, 42 Dubois, Y., Gavazzi, R., Peirani, S., & Silk, J. 2013, ArXiv e-prints

Dutton, A. A., & Treu, T. 2013, ArXiv e-prints

Faber, S. M., Phillips, A. C., Kibrick, R. I., Alcott, B., Allen, S. L., Burrous, J., Cantrall, T., Clarke, D., Coil, A. L., Cowley, D. J., Davis, M., Deich, W. T. S., Dietsch, K., Gilmore, D. K., Harper, C. A., Hilyard, D. F., Lewis, J. P., McVeigh, M., Newman, J., Osborne, J., Schiavon, R., Stover, R. J., Tucker, D., Wallace, V., Wei, M., Wirth, G., & Wright, C. A. 2003, in Society of Photo-Optical Instrumentation Engineers (SPIE) Conference Series, Vol. 4841, Society of Photo-Optical Instrumentation Engineers (SPIE) Conference Series, ed. M. Iye & A. F. M. Moorwood, 1657–1669

Faure, C., Kneib, J.-P., Covone, G., Tasca, L., Leauthaud, A.,
Capak, P., Jahnke, K., Smolcic, V., de la Torre, S., Ellis, R.,
Finoguenov, A., Koekemoer, A., Le Fevre, O., Massey, R.,
Mellier, Y., Refregier, A., Rhodes, J., Scoville, N., Schinnerer,
E., Taylor, J., Van Waerbeke, L., & Walcher, J. 2008, ApJS,
176, 19

Ferrarese, L., & Merritt, D. 2000, ApJ, 539, L9

Gavazzi, R., Treu, T., Marshall, P. J., Brault, F., & Ruff, A. 2012, ApJ, 761, 170

Gavazzi, R., Treu, T., Rhodes, J. D., Koopmans, L. V. E., Bolton, A. S., Burles, S., Massey, R. J., & Moustakas, L. A. 2007, ApJ, 667, 176

Gebhardt, K., Bender, R., Bower, G., Dressler, A., Faber, S. M., Filippenko, A. V., Green, R., Grillmair, C., Ho, L. C., Kormendy, J., Lauer, T. R., Magorrian, J., Pinkney, J., Richstone, D., & Tremaine, S. 2000, ApJ, 539, L13

González-Nuevo, J., Lapi, A., Fleuren, S., Bressan, S., Danese, L., De Zotti, G., Negrello, M., Cai, Z.-Y., Fan, L., Sutherland, W., Baes, M., Baker, A. J., Clements, D. L., Cooray, A., Dannerbauer, H., Dunne, L., Dye, S., Eales, S., Frayer, D. T., Harris, A. I., Ivison, R., Jarvis, M. J., Michałowski, M. J., López-Caniego, M., Rodighiero, G., Rowlands, K., Serjeant, S., Scott, D., van der Werf, P., Auld, R., Buttiglione, S., Cava, A., Dariush, A., Fritz, J., Hopwood, R., Ibar, E., Maddox, S., Pascale, E., Pohlen, M., Rigby, E., Smith, D., & Temi, P. 2012, ApJ, 749, 65

Hopkins, P. F., Bundy, K., Hernquist, L., Wuyts, S., & Cox, T. J. 2010, MNRAS, 401, 1099

Huertas-Company, M., Mei, S., Shankar, F., Delaye, L., Raichoor, A., Covone, G., Finoguenov, A., Kneib, J. P., Le, F. O., & Povic, M. 2013, MNRAS, 428, 1715

Ilbert, O., McCracken, H. J., Le Fevre, O., Capak, P., Dunlop, J., Karim, A., Renzini, M. A., Caputi, K., Boissier, S., Arnouts, S., Aussel, H., Comparat, J., Guo, Q., Hudelot, P., Kartaltepe, J., Kneib, J. P., Krogager, J. K., Le Floc'h, E., Lilly, S., Mellier, Y., Milvang-Jensen, B., Moutard, T., Onodera, M., Richard, J., Salvato, M., Sanders, D. B., Scoville, N., Silverman, J., Taniguchi, Y., Tasca, L., Thomas, R., Toft, S., Tresse, L., Vergani, D., Wolk, M., & Zirm, A. 2013, ArXiv e-prints

Inada, N., Oguri, M., Shin, M.-S., Kayo, I., Strauss, M. A., Morokuma, T., Rusu, C. E., Fukugita, M., Kochanek, C. S., Richards, G. T., Schneider, D. P., York, D. G., Bahcall, N. A. Frieman, J. A., Hall, P. B., & White, R. L. 2012, AJ, 143, 119 Jiang, G., & Kochanek, C. S. 2007, ApJ, 671, 1568

Johansson, P. H., Naab, T., & Ostriker, J. P. 2012, ApJ, 754, 115 Jørgensen, I., Franx, M., & Kjaergaard, P. 1995, MNRAS, 276, 1341

Kaviraj, S. 2010, MNRAS, 408, 170

Kelly, B. C. 2007, ApJ, 665, 1489

Koopmans, L. V. E., Bolton, A., Treu, T., Czoske, O., Auger, M. W., Barnabè, M., Vegetti, S., Gavazzi, R., Moustakas, L. A., & Burles, S. 2009, ApJ, 703, L51

Koopmans, L. V. E., & Treu, T. 2003, ApJ, 583, 606 Koopmans, L. V. E., Treu, T., Bolton, A. S., Burles, S., & Moustakas, L. A. 2006, ApJ, 649, 599

Lagattuta, D. J., Fassnacht, C. D., Auger, M. W., Marshall, P. J., Bradač, M., Treu, T., Gavazzi, R., Schrabback, T., Faure, C., & Anguita, T. 2010, ApJ, 716, 1579

Lin, Y.-T., Brodwin, M., Gonzalez, A. H., Bode, P., Eisenhardt, P. R. M., Stanford, S. A., & Vikhlinin, A. 2013, ApJ, 771, 61 Malin, D. F., & Carter, D. 1983, ApJ, 274, 534

Marshall, P. J., Hogg, D. W., Moustakas, L. A., Fassnacht, C. D., Bradač, M., Schrabback, T., & Blandford, R. D. 2009, ApJ, 694, 924

Navarro, J. F., Frenk, C. S., & White, S. D. M. 1997, ApJ, 490,

Negrello, M., Hopwood, R., De Zotti, G., Cooray, A., Verma, A., Bock, J., Frayer, D. T., Gurwell, M. A., Omont, A., Neri, R., Dannerbauer, H., Leeuw, L. L., Barton, E., Cooke, J., Kim, S., da Cunha, E., Rodighiero, G., Cox, P., Bonfield, D. G., Jarvis, M. J., Serjeant, S., Ivison, R. J., Dye, S., Aretxaga, I., Hughes, D. H., Ibar, E., Bertoldi, F., Valtchanov, I., Eales, S., Dunne, L., Driver, S. P., Auld, R., Buttiglione, S., Cava, A., Grady, C. A., Clements, D. L., Dariush, A., Fritz, J., Hill, D., Hornbeck, J. B., Kelvin, L., Lagache, G., Lopez-Caniego, M., Gonzalez-Nuevo, J., Maddox, S., Pascale, E., Pohlen, M., Rigby, E. E., Robotham, A., Simpson, C., Smith, D. J. B., Temi, P., Thompson, M. A., Woodgate, B. E., York, D. G., Aguirre, J. E., Beelen, A., Blain, A., Baker, A. J., Birkinshaw, M., Blundell, R., Bradford, C. M., Burgarella, D., Danese, L., Dunlop, J. S., Fleuren, S., Glenn, J., Harris, A. I., Kamenetzky, J., Lupu, R. E., Maddalena, R. J., Madore, B. F., Maloney, P. R., Matsuhara, H., Michaowski, M. J., Murphy, E. J., Naylor, B. J., Nguyen, H., Popescu, C., Rawlings, S., Rigopoulou, D., Scott, D., Scott, K. S., Seibert, M., Smail, I., Tuffs, R. J., Vieira, J. D., van der Werf, P. P., & Zmuidzinas, J. 2010, Science, 330, 800

Newman, J. A., Cooper, M. C., Davis, M., Faber, S. M., Coil, A. L., Guhathakurta, P., Koo, D. C., Phillips, A. C., Conroy, C., Dutton, A. A., Finkbeiner, D. P., Gerke, B. F., Rosario, D. J., Weiner, B. J., Willmer, C. N. A., Yan, R., Harker, J. J., Kassin, S. A., Konidaris, N. P., Lai, K., Madgwick, D. S., Noeske, K. G., Wirth, G. D., Connolly, A. J., Kaiser, N., Kirby, E. N., Lemaux, B. C., Lin, L., Lotz, J. M., Luppino, G. A., Marinoni, C., Matthews, D. J., Metevier, A., & Schiavon, R. P. 2012, ArXiv e-prints

Nipoti, C., Treu, T., Auger, M. W., & Bolton, A. S. 2009a, ApJ, 706, L86

Nipoti, C., Treu, T., & Bolton, A. S. 2009b, ApJ, 703, 1531 Nipoti, C., Treu, T., Leauthaud, A., Bundy, K., Newman, A. B., & Auger, M. W. 2012, MNRAS, 422, 1714

Oke, J. B., Cohen, J. G., Carr, M., Cromer, J., Dingizian, A., Harris, F. H., Labrecque, S., Lucinio, R., Schaal, W., Epps, H., & Miller, J. 1995, PASP, 107, 375

Oser, L., Naab, T., Ostriker, J. P., & Johansson, P. H. 2012, ApJ, 744, 63

Pawase, R. S., Faure, C., Courbin, F., Kokotanekova, R., & Meylan, G. 2012, ArXiv e-prints

Poggianti, B. M., Calvi, R., Bindoni, D., D'Onofrio, M., Moretti, A., Valentinuzzi, T., Fasano, G., Fritz, J., De Lucia, G., Vulcani, B., Bettoni, D., Gullieuszik, M., & Omizzolo, A. 2013, ApJ, 762, 77

Remus, R.-S., Burkert, A., Dolag, K., Johansson, P. H., Naab, T., Oser, L., & Thomas, J. 2013, ApJ, 766, 71

Renzini, A. 2006, ARA&A, 44, 141

Rockosi, C., Stover, R., Kibrick, R., Lockwood, C., Peck, M., Cowley, D., Bolte, M., Adkins, S., Alcott, B., Allen, S. L., Brown, B., Cabak, G., Deich, W., Hilyard, D., Kassis, M., Lanclos, K., Lewis, J., Pfister, T., Phillips, A., Robinson, L., Saylor, M., Thompson, M., Ward, J., Wei, M., & Wright, C. 2010, in Society of Photo-Optical Instrumentation Engineers (SPIE) Conference Series, Vol. 7735, Society of Photo-Optical Instrumentation Engineers (SPIE) Conference Series

Ruff, A. J., Gavazzi, R., Marshall, P. J., Treu, T., Auger, M. W., & Brault, F. 2011, ApJ, 727, 96

Rusin, D., & Kochanek, C. S. 2005, ApJ, 623, 666

Rusin, D., Kochanek, C. S., & Keeton, C. R. 2003, ApJ, 595, 29 Sonnenfeld, A., Treu, T., Gavazzi, R., Marshall, P. J., Auger, M. W., Suyu, S. H., Koopmans, L. V. E., & Bolton, A. S. 2012, ApJ, 752, 163

Sonnenfeld, A., Treu, T., Gavazzi, R., Suyu, S. H., & Marshall, P. J. 2013, submitted to ApJ, available at

http://web.physics.ucsb.edu/~sonnen/SL2S-III.pdf Suyu, S. H., Marshall, P. J., Auger, M. W., Hilbert, S., Blandford, R. D., Koopmans, L. V. E., Fassnacht, C. D., & Treu, T. 2010, ApJ, 711, 201

Tal, T., van Dokkum, P. G., Nelan, J., & Bezanson, R. 2009, AJ, 138, 1417

Treu, T., Auger, M. W., Koopmans, L. V. E., Gavazzi, R., Marshall, P. J., & Bolton, A. S. 2010, ApJ, 709, 1195

Treu, T., Dutton, A. A., Auger, M. W., Marshall, P. J., Bolton, A. S., Brewer, B. J., Koo, D. C., & Koopmans, L. V. E. 2011, MNRAS, 417, 1601

Treu, T., & Koopmans, L. V. E. 2002a, ApJ, 575, 87 —. 2002b, MNRAS, 337, L6

-. 2004, ApJ, 611, 739

Treu, T., Stiavelli, M., Casertano, S., Møller, P., & Bertin, G. $2002,\,\mathrm{ApJ},\,564,\,\mathrm{L}13$

van der Marel, R. P. 1994, MNRAS, 270, 271

van Dokkum, P. G. 2005, AJ, 130, 2647

van Dokkum, P. G., & Conroy, C. 2010, Nature, 468, 940 van Dokkum, P. G., Franx, M., Kriek, M., Holden, B., Illingworth, G. D., Magee, D., Bouwens, R., Marchesini, D., Quadri, R., Rudnick, G., Taylor, E. N., & Toft, S. 2008, ApJ, 677, L5

Vieira, J. D., Marrone, D. P., Chapman, S. C., De Breuck, C., Hezaveh, Y. D., Weiβ, A., Aguirre, J. E., Aird, K. A., Aravena, M., Ashby, M. L. N., Bayliss, M., Benson, B. A., Biggs, A. D., Bleem, L. E., Bock, J. J., Bothwell, M., Bradford, C. M., Brodwin, M., Carlstrom, J. E., Chang, C. L., Crawford, T. M., Crites, A. T., de Haan, T., Dobbs, M. A., Fomalont, E. B., Fassnacht, C. D., George, E. M., Gladders, M. D., Gonzalez, A. H., Greve, T. R., Gullberg, B., Halverson, N. W., High, F. W., Holder, G. P., Holzapfel, W. L., Hoover, S., Hrubes, J. D., Hunter, T. R., Keisler, R., Lee, A. T., Leitch, E. M., Lueker, M., Luong-van, D., Malkan, M., McIntyre, V., McMahon, J. J., Mehl, J., Menten, K. M., Meyer, S. S. Mocanu, L. M., Murphy, E. J., Natoli, T., Padin, S., Plagge, T., Reichardt, C. L., Rest, A., Ruel, J., Ruhl, J. E., Sharon, K., Schaffer, K. K., Shaw, L., Shirokoff, E., Spilker, J. S., Stalder, B., Staniszewski, Z., Stark, A. A., Story, K., Vanderlinde, K., Welikala, N., & Williamson, R. 2013, Nature, 495, 344

Wardlow, J. L., Cooray, A., De Bernardis, F., Amblard, A., Arumugam, V., Aussel, H., Baker, A. J., Béthermin, M., Blundell, R., Bock, J., Boselli, A., Bridge, C., Buat, V., Burgarella, D., Bussmann, R. S., Cabrera-Lavers, A., Calanog, J., Carpenter, J. M., Casey, C. M., Castro-Rodríguez, N., Cava, A., Chanial, P., Chapin, E., Chapman, S. C., Clements, D. L., Conley, A., Cox, P., Dowell, C. D., Dye, S., Eales, S., Farrah, D., Ferrero, P., Franceschini, A., Frayer, D. T., Frazer, C., Fu, H., Gavazzi, R., Glenn, J., González Solares, E. A., Griffin, M., Gurwell, M. A., Harris, A. I., Hatziminaoglou, E., Hopwood, R., Hyde, A., Ibar, E., Ivison, R. J., Kim, S., Lagache, G., Levenson, L., Marchetti, L., Marsden, G., Martinez-Navajas, P., Negrello, M., Neri, R., Nguyen, H. T., O'Halloran, B., Oliver, S. J., Omont, A., Page, M. J., Panuzzo, P., Papageorgiou, A., Pearson, C. P., Pérez-Fournon, I., Pohlen, M., Riechers, D., Rigopoulou, D., Roseboom, I. G., Rowan-Robinson, M., Schulz, B., Scott, D., Scoville, N., Seymour, N., Shupe, D. L., Smith, A. J., Streblyanska, A., Strom, A., Symeonidis, M., Trichas, M., Vaccari, M., Vieira, J. D., Viero, M., Wang, L., Xu, C. K., Yan, L., & Zemcov, M. 2013, ApJ, 762, 59